



Publication Year	2020
Acceptance in OA	2025-02-18T10:33:34Z
Title	Carbon isotopic fractionation in molecular clouds
Authors	Colzi, L., Sipilä, O., Roueff, E., Caselli, P., FONTANI, Francesco
Publisher's version (DOI)	10.1051/0004-6361/202038251
Handle	http://hdl.handle.net/20.500.12386/36025
Journal	ASTRONOMY & ASTROPHYSICS
Volume	640

Carbon isotopic fractionation in molecular clouds

L. Colzi^{1,2}, O. Sipilä³, E. Roueff⁴, P. Caselli³, and F. Fontani²

¹ Università degli studi di Firenze, Dipartimento di fisica e Astronomia, Via Sansone 1, 50019 Sesto Fiorentino, Italy
e-mail: lcolzi.astro@gmail.com, laura.colzi@unifi.it

² INAF – Osservatorio Astrofisico di Arcetri, Largo E. Fermi 5, 50125 Florence, Italy

³ Max-Planck-Institut für extraterrestrische Physik, Giessenbachstrasse 1, 85748 Garching bei München, Germany

⁴ Sorbonne Université, Observatoire de Paris, Université PSL, CNRS, LERMA, 92190 Meudon, France

Received 24 April 2020 / Accepted 4 June 2020

ABSTRACT

Context. Carbon fractionation has been studied from a theoretical point of view with different models of time-dependent chemistry, including both isotope-selective photodissociation and low-temperature isotopic exchange reactions.

Aims. Recent chemical models predict that isotopic exchange reactions may lead to a depletion of ¹³C in nitrile-bearing species, with ¹²C/¹³C ratios two times higher than the elemental abundance ratio of 68 in the local interstellar medium. Since the carbon isotopic ratio is commonly used to evaluate the ¹⁴N/¹⁵N ratios with the double-isotope method, it is important to study carbon fractionation in detail to avoid incorrect assumptions.

Methods. In this work, we implemented a gas-grain chemical model with new isotopic exchange reactions and investigated their introduction in the context of dense and cold molecular gas. In particular, we investigated the ¹²C/¹³C ratios of HNC, HCN, and CN using a grid of models, with temperatures and densities ranging from 10 to 50 K and 2×10^3 to 2×10^7 cm⁻³, respectively.

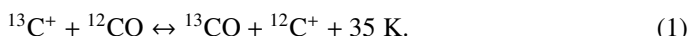
Results. We suggest a possible ¹³C exchange through the ¹³C + C₃ → ¹²C + ¹³CC₂ reaction, which does not result in dilution, but rather in ¹³C enhancement, for molecules that are formed starting from atomic carbon. This effect is efficient in a range of time between the formation of CO and its freeze-out on grains. Furthermore, the parameter-space exploration shows, on average, that the ¹²C/¹³C ratios of nitriles are predicted to be a factor 0.8–1.9 different from the local ¹²C/¹³C of 68 for high-mass star-forming regions. This result also affects the ¹⁴N/¹⁵N ratio: a value of 330 obtained with the double-isotope method is predicted to vary in the range 260–630, up to 1150, depending on the physical conditions. Finally, we studied the ¹²C/¹³C ratios of nitriles by varying the cosmic-ray ionisation rate, ζ : the ¹²C/¹³C ratios increase with ζ because of secondary photons and cosmic-ray reactions.

Key words. astrochemistry – methods: numerical – ISM: molecules – molecular processes

1. Introduction

Isotopic fractionation is an important chemical process that occurs in interstellar clouds. It is the set of processes that distribute the less abundant stable isotopes of an element into other molecular species. Understanding isotopic abundances over a large range of scales, from terrestrial oceans, meteorites, planetary, and cometary atmospheres up to Galactic and extragalactic environments is crucial. In particular, the variation in isotopic ratios may give important information about the link between Solar System objects and Galactic interstellar environments (e.g. Caselli & Ceccarelli 2012; Hily-Blant et al. 2013a,b; Ceccarelli et al. 2014; Fontani et al. 2015, 2020; Colzi et al. 2018a,b, 2019).

One element for which fractionation is important is carbon. C-fractionation in dense interstellar clouds has been studied with different models of time-dependent chemistry. Langer et al. (1984) introduced different isotopic exchange reactions in their model, as proposed by Watson et al. (1976). In particular, they proposed that C-fractionation in interstellar species is a result of the isotopic exchange reaction:



They concluded that the lower the temperature, the higher the chemical fractionation of C-bearing species. In fact, this reaction leads to a ¹³C enhancement in CO and to a dilution in species formed from C⁺ when all of the carbon is not fully locked in

CO. Smith & Adams (1980), under the suggestion of Langer et al. (1978), measured the rate coefficient for another isotopic exchange reaction:



with $\Delta E = 12 \pm 4$. However, more recently, this reaction was revised theoretically by Mladenović & Roueff (2014) who derived a value of 17.4 K from detailed zero-point energy (ZPE) calculations. This value is very similar to the one estimated by Hennig et al. (1977) of 17 ± 1 K. All of these reactions are very important in a low temperature (~20 K) environment.

In more recent works, fractionation effects due to the photodissociation of CO by ultraviolet (UV) photons, based on the theoretical studies by van Dishoeck & Black (1988), has been taken into account in chemical models. In particular, the selective photodissociation of ¹²CO is expected to be dominant in low-density (<10² cm⁻³) environments, or denser regions with a strong radiation field. Röllig & Ossenkopf (2013) found, with their photodissociation region (PDR) model, that ¹²CO/¹³CO is always equal to the ¹²C/¹³C elemental ratio (~68). However, Visser et al. (2009) were able, with their PDR model, to reproduce both higher and lower values with respect to the elemental ratio, as a function of H₂ column density. In fact, Visser et al. (2009) introduced Alfvén waves in their code, which have the effect of replacing the kinetic temperatures (T_{kin}) in the rate equation of ion-neutral reactions by an effective temperature that

takes into account these non-thermal effects. They demonstrated that these effects can take place and modify the $^{12}\text{C}/^{13}\text{C}$ ratio.

Observationally, numerous studies of the $^{12}\text{C}/^{13}\text{C}$ ratio have been conducted towards molecular clouds in the Galaxy, but most of them through observations of CO, H_2CO , and HCO^+ , which, as stated before, have the possible effects of isotopic-selective photodissociation and/or chemical fractionation (e.g. [Wilson & Rood 1994](#); [Langer & Penzias 1990, 1993](#)). To estimate the $^{12}\text{C}/^{13}\text{C}$ elemental ratio across the Galaxy, [Milam et al. \(2005\)](#) observed ^{12}CN and ^{13}CN towards Galactic molecular clouds. They found:

$$^{12}\text{C}/^{13}\text{C} = (6.01 \pm 1.19) \text{ kpc}^{-1} \times D_{\text{GC}} + (12.28 \pm 9.33). \quad (3)$$

Moreover, they also derived a galactocentric trend taking into account all together CN, CO, and H_2CO observations:

$$[^{12}\text{C}/^{13}\text{C}]_{\text{all molecules}} = (6.21 \pm 1.00) \text{ kpc}^{-1} \times D_{\text{GC}} + (18.71 \pm 10.88), \quad (4)$$

and then the average local present-day $^{12}\text{C}/^{13}\text{C}$ is 68 ± 15 (at a Sun distance $D_{\text{GC}} = 7.9$ kpc, as derived by [Hunt et al. 2016](#) and [Boehle et al. 2016](#)). In particular, the elemental $^{12}\text{C}/^{13}\text{C}$ ratio as a function of the galactocentric distance is determined by stellar nucleosynthesis processes. [Romano et al. \(2017\)](#) have shown that the observed trends are in agreement with Galactic chemical evolution models that include primary formation (i.e. starting from the primordial H and He nuclei) of ^{12}C in all stars and of ^{13}C in intermediate-mass asymptotic giant branch stars.

More recently, [Yan et al. \(2019\)](#) presented H_2CO and H_2^{13}CO observations towards a sample of 112 sources from which they evaluated a new $^{12}\text{C}/^{13}\text{C}$ trend as a function of D_{GC} . They obtained the following linear fit:

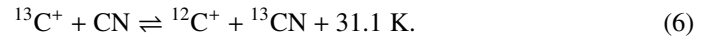
$$^{12}\text{C}/^{13}\text{C} = (5.08 \pm 1.10) \text{ kpc}^{-1} \times D_{\text{GC}} + (11.86 \pm 6.60), \quad (5)$$

which is consistent within the error bars with that found by [Milam et al. \(2005\)](#) (both Eqs. (3) and (4)). This indicates that even if H_2CO can be affected by chemical fractionation processes, either as a consequence of reactions (1) and (2) or of isotope-selective photodissociation effects (e.g. [Visser et al. 2009](#)), the trend with the galactocentric distance can still be disentangled from these effects.

[Daniel et al. \(2013\)](#) performed a non-local thermal-equilibrium analysis of HCN, HNC, CN, and their ^{13}C -isotopologues towards the pre-stellar core B1b. They found $\text{HNC}/\text{HN}^{13}\text{C} = 20_{-4}^{+5}$, $\text{HCN}/\text{H}^{13}\text{CN} = 30_{-4}^{+7}$, and $\text{CN}/^{13}\text{CN} = 50_{-11}^{+19}$. [Magalhães et al. \(2018\)](#) obtained, towards the starless core L1498, a $\text{HCN}/\text{H}^{13}\text{CN}$ ratio of 45 ± 3 . These works show that nitrile-bearing species are enriched in ^{13}C with respect to the local ISM value ($^{12}\text{C}/^{13}\text{C} = 68$).

Knowledge of the exact value of the $^{12}\text{C}/^{13}\text{C}$ ratio is also important for deriving the $^{14}\text{N}/^{15}\text{N}$ ratio for nitrile-bearing species since most studies use the so-called double isotope method (e.g. [Wampfler et al. 2014](#); [Zeng et al. 2017](#); [Colzi et al. 2018a,b](#)). This is based on observations of optically thin species, with ^{13}C substituted for ^{12}C (e.g. H^{13}CN , HN^{13}C). However, this method works only if the assumed $^{12}\text{C}/^{13}\text{C}$ ratio is comparable, within the errors, with the value given by the galactocentric trend, or if it can be determined independently from observations or chemical models. In fact, ^{13}C chemical fractionation may affect the abundances, and also the $^{14}\text{N}/^{15}\text{N}$ ratio, of nitrile-bearing species. This behaviour is typically not taken into account in chemical models inclusive of ^{15}N -bearing species.

Moreover, the observed $^{12}\text{C}/^{13}\text{C}$ abundance ratios listed above are not consistent with the values predicted by chemical models for species like CN, HCN, and HNC. As shown by [Roueff et al. \(2015\)](#), the dilution of ^{13}C for nitriles and isonitriles is at most a factor of 2 if derived from pure gas-phase chemical models with a fixed kinetic temperature of 10 K. However, these models do not include gas-grain interactions and introduce depletion effects by simply varying the elemental abundances of carbon, oxygen and nitrogen. It is thus important to test and refine the predictions of these models by introducing time dependent depletion effects resulting from gas-grain interactions. [Roueff et al. \(2015\)](#) also studied C-fractionation for C, CH, CO, and HCO^+ , showing that the $^{12}\text{C}/^{13}\text{C}$ ratio is highly time-dependent. In fact, since the start of the simulation, $^{13}\text{C}^+$ forms ^{13}CO through reaction (1). For a similar reason, CN is enriched in ^{13}C with similar timescales compared to ^{13}C -enrichment in CO, due to the reaction:



Reaction (2) becomes significant once $^{13}\text{C}^+$ starts to deplete from the gas phase. HCO^+ is then enriched in ^{13}C as long as the ^{13}CO remains in excess with respect to ^{12}CO (i.e. until $\text{CO}/^{13}\text{CO}$ comes back to the initial value of 68). The gas-phase chemical model of [Roueff et al. \(2015\)](#) reached a steady state at about 10^7 yr for a density of $2 \times 10^4 \text{ cm}^{-3}$. At this time C, CH, HCN, HNC, and CN are depleted in ^{13}C . This is related to reactions (1) and (2) that continue to be important and retain all the ^{13}C in CO and HCO^+ .

In this work, we report a new detailed analysis of the $^{12}\text{C}/^{13}\text{C}$ ratio derived under different fixed physical conditions, and with the introduction of new low-temperature isotopic exchange reactions. We first describe the gas-grain chemical model and the network used (Sect. 2). Then, we present the fiducial model that we have chosen to describe the main characteristics and new results about C-fractionation of this chemical model (Sect. 3.1). Finally, we present and discuss a parameter-space exploration for CN, HCN, and HNC. We show how the C-fractionation in some specific models varies with the density, the temperature and the cosmic-ray ionisation rate. We also describe the link with the $^{14}\text{N}/^{15}\text{N}$ derived towards high-mass star-forming regions with the double-isotope method (Sect. 3.2).

2. Model

2.1. Chemical model

Our chemical code is based on the one described in [Sipilä et al. \(2015a\)](#), recently updated to include several new chemical processes ([Sipilä et al. 2019b](#)). In short, the code solves rate equations for gas-phase and grain-surface chemistry, which are connected through adsorption and (non-)thermal desorption. A description of the basic processes including relevant equations can be found in [Sipilä et al. \(2015a\)](#) and are not reproduced here for the sake of brevity.

2.2. Introduction of ^{13}C -fractionation in the chemical model

In this paper, we model the isotopic fractionation of carbon by introducing the isotope ^{13}C to the KIDA gas-phase network ([Wakelam et al. 2015](#)) using a procedure similar to our earlier approach to generating deuterated networks ([Sipilä et al. 2013](#); [Sipilä et al. 2015b](#)).

As an example of the fractionation-generation procedure, we consider the reaction

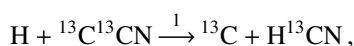
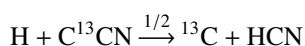
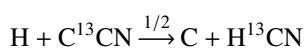


Here, the ^{13}C atom can be introduced in CCN in two positions that are considered equivalent. From a chemical standpoint, the position of the ^{13}C atom is important and may impact the reactivity of the molecule, but here we make the simplifying assumption that the order of carbon atoms does not need to be tracked. We note, however, that significant differences in abundances have been observed for molecules where the ^{13}C atom can be located in different positions. For example, Sakai et al. (2010) observed the $N=1-0$ lines of CCH and its ^{13}C -isotopic species towards the dark cloud TMC-1 and the star-forming region L1527. They investigated the ^{13}C -species abundances and the possible different formation pathways. They found a $\text{C}^{13}\text{CH}/^{13}\text{CCH}$ ratio of 1.6 ± 0.4 and 1.6 ± 0.1 towards TMC-1 and L1527, respectively. They proposed that the reaction



could make a difference between the formation of the two ^{13}C -isotopic species of C_2H . Taniguchi et al. (2019) found similar results towards L1521B and L134N. However, testing this result is beyond the scope of this work.

According to our present approach, the following branches will be generated once ^{13}C is substituted in reaction (7):



where the branching ratio is displayed above the arrow. Essentially, we calculate the probability of a given branch based on the positions that the ^{13}C atom can occupy on the product side of the reaction. The same rule is applied to most reactions, meaning the inherent assumption is that the reactions proceed via full scrambling, which is not universally true (Sipilä et al. 2019a). Notable exceptions to the full-scrambling rule are charge-exchange reactions and proton-donation reactions that involve at least one carbon atom in each reactant and product. For these reactions, we assume that carbon atoms cannot be interchanged in the reaction. Mass and/or energy corrections to the rate coefficients of the reactions due to isotopic effects are expected to be small, below the expected accuracy of the reaction rate coefficients, except for possible isotopic exchange reactions, as discussed in Sect. 2.3. The same fractionation procedure is applied to our grain-surface network (Sipilä et al. 2019b).

We do not consider fractionation for all carbon-containing reactions included in KIDA, or in our surface network, in order to maintain relative simplicity while still including the chemistry that is essential for the molecules typically observed and used to derive fractionation ratios. First, we discarded all reactions that contain molecules with more than five atoms. So, for example, cyanoacetylene (HC_3N) is included in our models, while methanol (CH_3OH) is not. In Sect. 3, we discuss the results on diatomic and triatomic molecules, which should not be affected too much by this restriction. Second, we only performed the fractionation procedure for reactions that contain molecules with up to three carbon atoms, and so our final networks do not contain species like C_3^{13}CH . With these restrictions, our final networks (gas-phase and grain-surface) contain a combined total of $\sim 11\,500$ reactions. Appendix A.1 describes the possible issues in the building of the isotopic chemistry and compares the present method to that used in Roueff et al. (2015).

2.3. Isotopic exchange reactions

In this work, we examine the behaviour of C-fractionation in a low-temperature environment ($T_{\text{gas}} \leq 50$ K). Isotopic exchange reactions are very important in these cold regions and could affect the behaviour of the $^{12}\text{C}/^{13}\text{C}$ ratio in different molecules. Roueff et al. (2015) studied the $^{12}\text{C}/^{13}\text{C}$ ratio of some molecules, introducing some isotopic exchange reactions. For this work, we updated the list of exchange reactions, as shown in Table 1. These reactions can occur in the absence of potential barriers and when no other exothermic product channel is available.

We now discuss the new suggested reactions shown in the bottom panel of Table 1. To quantify the efficiency of these possible exchange reactions, we computed the variation of the involved ZPE, and we assumed that the reactions take place via an intermediate complex.

Since no experimental data is available, we assumed a pre-exponential factor. For ion-neutral reactions, we could use the rate given by the Langevin formula:

$$k_{\text{AB}} = 2.34 \times 10^{-09} q \left(\frac{\alpha}{\mu} \right)^{1/2} \text{ cm}^3 \text{ s}^{-1}, \quad (9)$$

where μ is the reduced mass of the reactants in atomic mass units (amu), q is the electronic charge, and α is the polarisability of the neutral species in cubic angstroms. However, since this expression represents an upper limit for the reaction probability, we decided to guess the rate coefficients, setting them to a similar order of magnitude with previously known reaction. Reactions involving the C^+ ion and a diatomic molecule (6, 7, and 9 of Table 1) are assumed to proceed at the Langevin rate. However, the $\text{C}^+ + \text{C}_3$ reaction could lead to different products, depending on the carbon position. For this, we assumed a rate of $9.5 \times 10^{-10} \text{ cm}^3 \text{ s}^{-1}$, about half of the Langevin rate ($1.7 \times 10^{-9} \text{ cm}^3 \text{ s}^{-1}$). We made this assumption since in this work we consider only one position ($^{13}\text{C}^{12}\text{C}_2$). Exchange reactions may occur in neutral-neutral reactions. In the absence of more detailed theoretical investigations, for reactions (8) and (10) we assumed the same pre-exponential factor as for reaction (5) in Table 1. Moreover, for the new reactions studied in this work, the factor f is near unity unless C_2 (or C_3) appears, in which case it is ~ 2.0 if the symmetric molecule C_2 (or C_3) is a reactant, and ~ 0.5 if C_2 is a product, according to the symmetry factor term present in the partition function.

The exponential term $\exp(-\Delta E/T)$, which is both present in the forward reaction rate coefficients (except for reaction (2)) and in the reverse (endothermic) ones, requires the knowledge of the energy defect (ΔZPE), which is obtained from the difference of the zero-point energies of the products and the reactants. In Table 2, we report the difference in zero-point energies between the more and less abundant isotopologues found in the literature for C_2 , CS, and C_3 . The energies involved depend on the position of ^{13}C , as indicated in Table 2. As we did not track the position of ^{13}C , we take the lowest value involved for the energy defect, making it possible to evaluate the importance of this mechanism at its minimum level. ^{13}C -fractionation in C_3 could proceed further through reaction of ^{13}C with $^{13}\text{CC}_2$ and other ^{13}C substituents. We carried out some tests that showed that the effect of multiple ^{13}C -fractionation on our results is negligible. We leave the full study for future considerations.

3. Results and discussion

In this section, we discuss the main results obtained with the simulation at different densities and temperatures. The main physical

Table 1. Carbon isotopic exchange reactions used in this work.

Label	Reaction	k_f ($\text{cm}^3 \text{s}^{-1}$)	$f(B, m)^{(a)}$	$\Delta E^{(b)}$ (K)
(1) B	$^{13}\text{C}^+ + \text{CO} \rightleftharpoons ^{12}\text{C}^+ + ^{13}\text{CO}$	$6.6 \times 10^{-10} \times \left(\frac{T}{300}\right)^{-0.45} \times \exp(-6.5/T) \times \frac{1}{1+\exp(-34.7/T)}$	1	34.7
(2) A	$^{13}\text{CO} + \text{HCO}^+ \rightleftharpoons \text{CO} + \text{H}^{13}\text{CO}^+$	$2.6 \times 10^{-12} \times \left(\frac{T}{300}\right)^{-0.4}$	1	17.4
(3) B	$^{13}\text{C}^+ + \text{CN} \rightleftharpoons ^{12}\text{C}^+ + ^{13}\text{CN}$	$3.82 \times 10^{-9} \times \left(\frac{T}{300}\right)^{-0.4} \times \frac{1}{1+\exp(-31.1/T)}$	1	31.1
(4) B	$^{13}\text{C} + \text{CN} \rightleftharpoons ^{12}\text{C} + ^{13}\text{CN}$	$3.0 \times 10^{-10} \times \frac{1}{1+\exp(-31.1/T)}$	1	31.1
(5) B	$^{13}\text{C} + \text{C}_2 \rightleftharpoons ^{12}\text{C} + ^{13}\text{CC}$	$3.0 \times 10^{-10} \times \frac{2}{2+\exp(-25.9/T)}$	2	25.9
(6) B	$^{13}\text{C}^+ + \text{C}_2 \rightleftharpoons ^{12}\text{C}^+ + ^{13}\text{CC}$	$1.86 \times 10^{-09} \times \frac{2}{2+\exp(-25.9/T)}$	2	25.9
(7) B	$^{13}\text{C}^+ + ^{13}\text{CC} \rightleftharpoons ^{12}\text{C}^+ + ^{13}\text{C}_2$	$1.86 \times 10^{-09} \times \frac{0.5}{0.5+\exp(-26.4/T)}$	0.5	26.4
(8) B	$^{13}\text{C} + ^{13}\text{CC} \rightleftharpoons ^{12}\text{C} + ^{13}\text{C}_2$	$3.0 \times 10^{-10} \times \frac{0.5}{0.5+\exp(-26.4/T)}$	0.5	26.4
(9) B	$^{13}\text{C}^+ + \text{CS} \rightleftharpoons ^{12}\text{C}^+ + ^{13}\text{CS}$	$1.86 \times 10^{-09} \times \frac{1}{1+\exp(-26.3/T)}$	1	26.3
(10) B	$^{13}\text{C} + \text{C}_3 \rightleftharpoons ^{12}\text{C} + ^{13}\text{CC}_2$	$3.0 \times 10^{-10} \times \frac{2}{2+\exp(-27/T)}$	2	27
(11) B	$^{13}\text{C}^+ + \text{C}_3 \rightleftharpoons ^{12}\text{C}^+ + ^{13}\text{CC}_2$	$9.5 \times 10^{-10} \times \frac{2}{2+\exp(-27/T)}$	2	27

Notes. The top panel displays the reactions already used by Roueff et al. (2015), while the bottom panel displays the reactions added for the present study. Type A reactions are direct reactions, while type B reactions are those involving adduct formation, without isomerisation, as defined by Roueff et al. (2015). $^{(a)}f(B, m)$ is a probability factor that depends on the rotational constant, mass, and symmetry factors of the reactants and products. In reactions involving ^{13}C , the mass ratio of the reactants and the products is close to unity. Then, $f(B, m) = q(\text{C})q(\text{D})/q(\text{A})q(\text{B})$, where A and B are the reactants, C and D the products, and $q(\dots)$ are the internal molecular partition functions. $^{(b)}\Delta E$ is the exoergicity of the reaction.

Table 2. Values of the ZPEs for molecules related to the isotopic exchange reactions used in our model.

Molecule	ZPE (cm^{-1})	$\Delta\text{ZPE}^{(a)}$ (K)	Reference
C_2	924.13	–	(1)
^{13}CC	906.1	25.9	(1)
$^{13}\text{C}_2$	887.8	52.3	(1)
$^{13}\text{C}_2^{(b)}$		26.4	(1)
CS	640.9	–	(2)
^{13}CS	622.7	26.3	(3)
C_3	1705.06	–	(4)
$^{13}\text{CC}_2$	1686.44	27	(4)
C^{13}CC	1675.54	43	(4)
$^{13}\text{CC}^{13}\text{C}^{(b)}$	1667.74	27	(4)
$^{13}\text{C}^{13}\text{CC}^{(b)}$	1656.70	43	(4)
$^{13}\text{C}_3^{(c)}$	1637.79	27	(4)

Notes. The related references are also given in the fourth column. $^{(a)}\Delta\text{ZPE}$ is equal to ΔE used in Table 1. $^{(b)}\Delta\text{ZPE}$ is derived with respect to the second molecular species of the group. $^{(c)}\Delta\text{ZPE}$ is derived with respect to the fifth molecular species of the group.

References. (1) Zhang et al. (2011); (2) Bergeman & Cossart (1981); (3) Huber & Herzberg (1979); (4) Schröder & Sebald (2016).

parameters that the chemical code requires are the total number density of H nuclei (n_{H}^1), the dust temperature (T_{dust}), the gas temperature (T_{gas}), the cosmic-ray ionisation rate (ζ), the visual

¹ $n_{\text{H}} = n(\text{H}) + 2n(\text{H}_2) \approx 2n(\text{H}_2)$ in dense molecular clouds like those simulated in this work.

Table 3. Values of the physical parameters fixed in each model.

Parameter	Value
ζ	$1.3 \times 10^{-17} \text{ s}^{-1}$
A_{V}	10 mag
ω	0.6
a_{g}	10^{-5} cm
ρ_{g}	3 g cm^{-3}
$\epsilon = E_{\text{diff}}/E_{\text{b}}$	0.6
$R_{\text{d}} = \text{dust-to-gas mass ratio}$	0.01

extinction (A_{V}), the grain albedo (ω), the grain radius (a_{g}), and the grain material density (ρ_{g}). The ratio between the diffuse and the binding energy of a species on dust grains (ϵ), and the dust-to-gas mass ratio (R_{g}). Apart from densities and temperatures, we fixed all of the other initial parameters as described in Table 3, except in Sect. 3.2.3 where we performed an analysis varying the cosmic-ray ionisation rate.

We assumed that the gas is initially atomic except for hydrogen, which is in molecular form. The adopted initial abundances are presented in Table 4 and are used for all of the models presented in this work, assuming an initial $^{12}\text{C}/^{13}\text{C}$ ratio of 68.

3.1. The fiducial model

First of all, we analysed the behaviour of the abundances and $^{12}\text{C}/^{13}\text{C}$ ratios of different species for a particular model with a fixed temperature and density. We chose the one with $T_{\text{gas}} = 10 \text{ K}$ and $n_{\text{H}} = 2 \times 10^4 \text{ cm}^{-3}$ as our fiducial model. We note that we always assume that the gas and dust are thermally coupled, so that $T_{\text{gas}} = T_{\text{dust}}$.

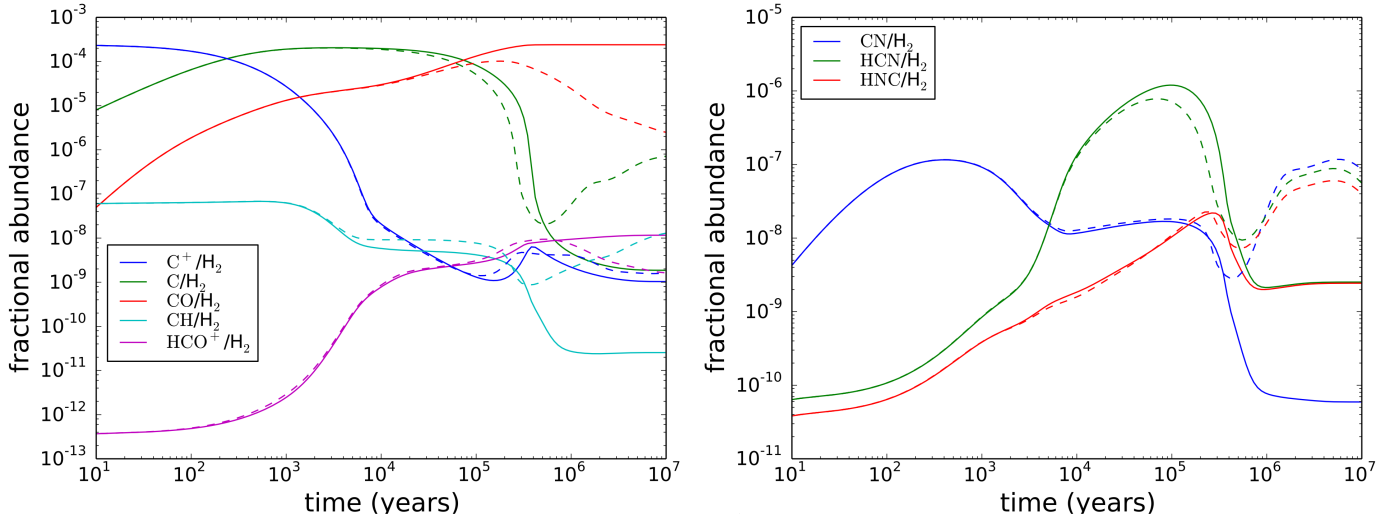


Fig. 1. Time evolution of C^+ , C, CO, CH, and HCO^+ (left panel) and of CN, HCN, and HNC (right panel) abundances with respect to H_2 for the fiducial model with only gas-phase chemistry at work (solid lines) and with both gas-phase and grain-surface chemistry at work (dashed lines).

Table 4. Initial abundances with respect to n_H .

Species	Initial abundance
H_2	0.5
He	9.00×10^{-2}
C^+	1.20×10^{-4}
$^{13}C^+$	1.76×10^{-6}
N	7.60×10^{-5}
O	2.56×10^{-4}
S^+	8.00×10^{-8}
Si^+	8.00×10^{-9}
Na^+	2.00×10^{-9}
Mg^+	7.00×10^{-9}
Fe^+	3.00×10^{-9}
P^+	2.00×10^{-10}
Cl^+	1.00×10^{-9}
F	2.00×10^{-9}

Notes. Adapted from Semenov et al. (2010). The initial ^{13}C abundance is given by $^{12}C/^{13}C = 68$.

3.1.1. Gas-phase model

Figure 1 shows the time-dependence of C^+ , C, CO, CH, HCO^+ , CN, HCN, and HNC abundances, for a model with only gas-phase chemistry at work (solid lines). Here, we simulated the formation of H_2 in the grain-surface $H + H$ association by constructing a dummy gas-phase reaction. The rate coefficient for this reaction, derived from the grain physical parameters reported in Table 3, is $\frac{1}{2}s\frac{3}{4}\frac{1.4m_H R_d}{\rho a_g}v_H n_H$, where s is the hydrogen sticking coefficient, m_H is the mass of the hydrogen atom, and v_H is the thermal speed of hydrogen (Le Petit et al. 2002). As in model (a) in Roueff et al. (2015), which corresponds to the same temperature, density and cosmic-ray ionisation rate, the steady-state is reached at a few million years. At the beginning, all the carbon is in ionised form, and after 10^2 yr it is converted into atomic carbon, which is later transformed into CO (in a

timescale of $\sim 10^5$ yr). Meanwhile, CH follows the behaviour of atomic carbon, and HCO^+ that of CO, as expected. In Fig. 2, the related $^{12}C/^{13}C$ ratios are shown with solid lines. As already explained in Sect. 1, the $^{12}C/^{13}C$ ratios of these molecules are mainly governed by the isotopic exchange reactions (1), (2), and (3) shown in Table 1. However, this model already shows differences between the results of Roueff et al. (2015) and this work. In fact, there is a range of time in which the $^{12}C/^{13}C$ ratios for nitrile-bearing species tend to be similar and lower than 68. These values for HCN and HNC were different and always higher than 68 in previous chemical models that simulated similar physical conditions (e.g. Roueff et al. 2015). As we discuss in Sect. 3.1.3, this behaviour is due to the introduction of the carbon isotopic exchange reaction of C_3 .

3.1.2. Gas-grain model

The time-dependence of C^+ , C, CO, CH, HCO^+ , CN, HCN, and HNC abundances, for the complete model, with both gas-phase and grain-surface reactions, is shown in Fig. 1 with dashed lines. In addition to what happens with a gas-phase-only model, after 2×10^5 yr, CO starts to freeze out on grain surfaces, and the abundance in the gas phase drops. Moreover, when most of the CO is depleted, the abundance of He^+ , which is produced at a constant rate by cosmic-ray-induced ionisation, increases as CO is one of its main destruction partner. He^+ continues to react with the remaining CO in the gas phase, increasing the abundance of C^+ . Moreover, as depletion occurs, C^+ mainly reacts with H_2 rather than with O-bearing species. This increases the CH abundance, and as a consequence, the abundance of related molecules such as C_2 , C_3 , CN, HCN, and HNC increases as well (Fig. 1 and left panel of Fig. 3). This behaviour was already predicted by Ruffle et al. (1997), and carbon chains such as HC_3N can be used as depletion indicators in late-type chemistry (after CO freeze-out).

Dashed lines in Fig. 2 display the time dependence of the $^{12}C/^{13}C$ ratios of the same molecules discussed above for the gas-phase model. For $t < 10^5$ yr, the inclusion of gas-grain interactions does not affect the isotopic ratio of C-bearing molecules. In fact, adsorption rates depend on v_i , the thermal speed of species i , which is inversely proportional to its mass. Since typical differences in mass between ^{12}C -containing species and

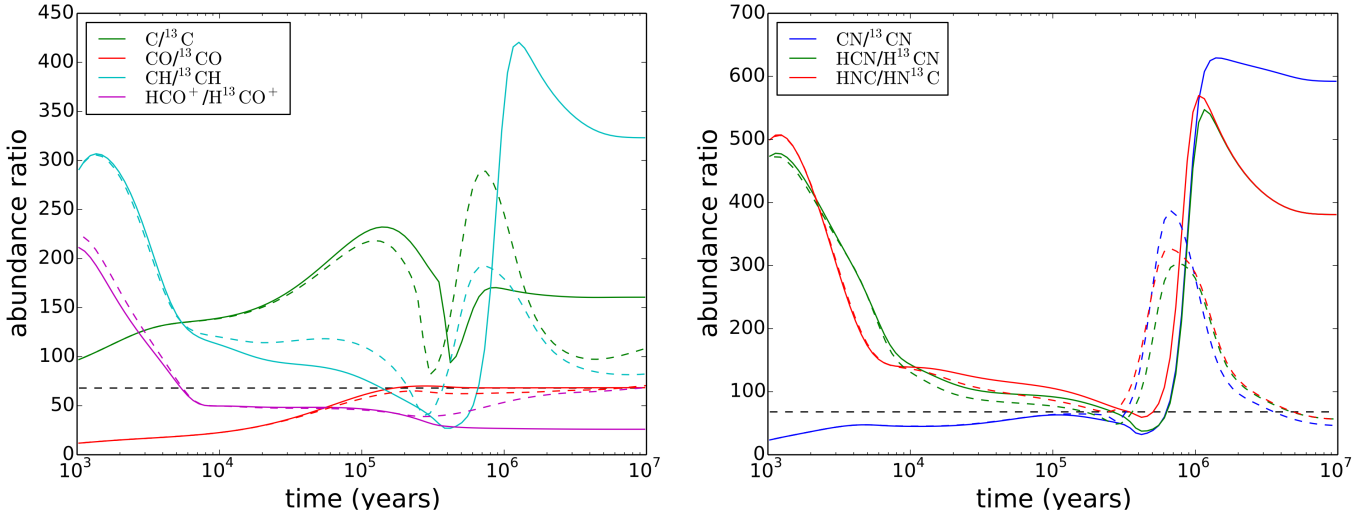


Fig. 2. Time evolution of the $^{12}\text{C}/^{13}\text{C}$ ratio for C, CO, CH, and HCO^+ (left panel), and for CN, HCN, and HNC (right panel) for the fiducial model with only gas-phase chemistry at work (solid lines) and with both gas-phase and grain-surface chemistry at work (dashed lines). In both panels, the black horizontal dashed line represents the initial $^{12}\text{C}/^{13}\text{C}$ ratio of 68.

^{13}C -containing species are less than a few percent, they do not have a significant effect. CO shows a ^{13}C -enhancement until the last million years of the time interval covered by the simulation. The $^{12}\text{C}/^{13}\text{C}$ ratios of C, CH, CN, HCN, and HNC peak at around 10^6 yr. The peak appears because of the interaction between gas and grains. In fact, during the fast early time chemistry most of the atomic carbon is transformed into CO. During this period, most of the ^{13}C is in principally in CO and, to a less extent, in HCO^+ , and is unavailable for other species. Then, after 10^6 yr, the $^{12}\text{C}/^{13}\text{C}$ ratios of the molecules listed above tend to decrease again because of the CO freeze-out that again drives atomic C to be the main reservoir of gas-phase carbon. Moreover, before 10^6 yr, there is a short interval of time where the $^{12}\text{C}/^{13}\text{C}$ ratios of C, CH, CN, HCN, and HNC tend to decrease, down to values lower than 68 (only for CH, CN and HCN), and after that timescale the ratios tend to increase again. We discuss below why this feature in the time dependence of $^{12}\text{C}/^{13}\text{C}$ ratio is present, and its consequences at different densities and temperatures.

In Appendix A.2, we compare the results obtained with our gas-grain chemistry with the ones obtained by Furuya et al. (2011). The results of the two chemical models are in agreement, and the differences are mainly due to the new low-temperature isotopic exchange reactions introduced in this work.

3.1.3. The importance of the possible C_3 isotopic exchange reaction

Observations of atomic carbon, and simple molecules containing more than one carbon atom, are important to put constraints on the processes that form larger molecules. The linear molecule C_3 is one of these species. It was observed for the first time in the ISM by Haffner & Meyer (1995), who reported a tentative detection, and then clearly by Maier et al. (2001). Later, Roueff et al. (2002) studied this molecule towards the diffuse molecular cloud HD 210121 where it forms mainly from the recombination of C_3H^+ and is destroyed by photodissociation. They found an abundance relative to H_2 of 6.75×10^{-9} . Other detections were made later towards stars surrounded by molecular clouds and in translucent sight lines (Galazutdinov et al. 2002; Ádámkóvics et al. 2003; Oka et al. 2003). Moreover, Wakelam et al. (2009) pointed out the possible occurrence of

radiative association of C_3 and C to form C_4 and the formation channel of CO through $\text{C}_4 + \text{O}$. They also pointed out that the reaction $\text{C} + \text{C}_5$ can be important for producing more C_3 and CO. Finally, Mookerjea et al. (2012) and Mookerjea et al. (2014) observed and modelled the abundance of C_3 towards envelopes of high-mass star-forming regions. Mookerjea et al. (2012) found an abundance of C_3 of $(6.3 \pm 1.3) \times 10^{-10}$ in the envelope towards DR1(OH), which they were able to reproduce with a chemical model with $n_{\text{H}_2} = 5 \times 10^6 \text{ cm}^{-3}$ and a temperature of 30 K. Mookerjea et al. (2014) observed along the line of sight of the UC HII region W51e2, with *Herschel*, detecting an absorption feature probably tracing a cold external envelope.

The carbon isotopic exchange reaction involving C_3 ,



was already emphasised in the discussion of the results displayed in Fig. 2. In this section, we investigate the contribution of this species to the $^{12}\text{C}/^{13}\text{C}$ ratio of different molecules. For this, we studied in detail the main reactions that form or destroy C_3 at two precise times in the fiducial model: 3×10^4 yr and 3×10^5 yr. These two times are earlier and later than the ‘early chemistry time’ (t_1), which we define as the time at which the abundance of atomic carbon drops by one order of magnitude while it is transformed into CO. In the fiducial model, $t_1 = 1.6 \times 10^5$ yr, and it is shown in Fig. 3 as the vertical purple line. Figure 3 displays the abundances (left panel) and the $^{12}\text{C}/^{13}\text{C}$ ratio (right panel) for CN, C, CO, C_2 , and C_3 . We note that the abundance of C_3 is two orders of magnitude higher than that of CN until the late-chemistry time, when CO starts to freeze out onto grain surfaces ($\sim 2\text{--}4 \times 10^5$ yr). The main reactions for the two times are summarised in Fig. 4 and are explained below in detail. Moreover, the $^{12}\text{C}/^{13}\text{C}$ ratio for some important molecules at the three times (3×10^4 yr, 1.6×10^5 yr, and 3×10^5 yr) are summarised in Table 5.

For $t < t_1$, $^{13}\text{CC}_2$ is enriched in ^{13}C , with respect to C_3 , thanks to the forward reaction (10). As a consequence, the $\text{C}_3/^{13}\text{CC}_2$ ratio is lower than the elemental initial value of 68, and the atomic $^{12}\text{C}/^{13}\text{C}$ is higher than 68. Even though reaction (6) has a similar exothermicity, reaction (10) is more efficient since $\text{C}_3/\text{H}_2 > \text{CN}/\text{H}_2$. This means that the $\text{C}_3/^{13}\text{CC}_2$ ratio is lower

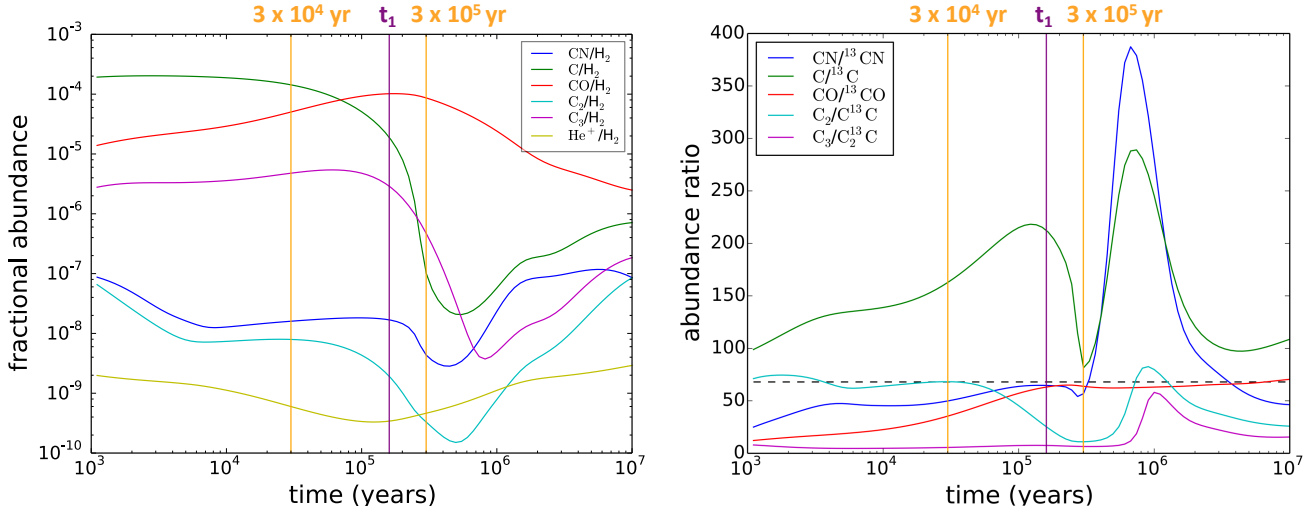


Fig. 3. *Left panel:* time evolution of CN, C, CO, C₂, C₃, and He⁺ abundances with respect to H₂ for the fiducial model. *Right panel:* time evolution of the ¹²C/¹³C for CN, C, CO, C₂, and C₃ for the fiducial model. The black horizontal dashed line represents the initial ¹²C/¹³C ratio of 68. In both panels, the vertical purple solid line represents the ‘early chemistry time’ as defined in the text, while the two vertical orange solid lines represent the two times (3×10^4 yr, and 3×10^5 yr) that we have analysed and discussed in the text.

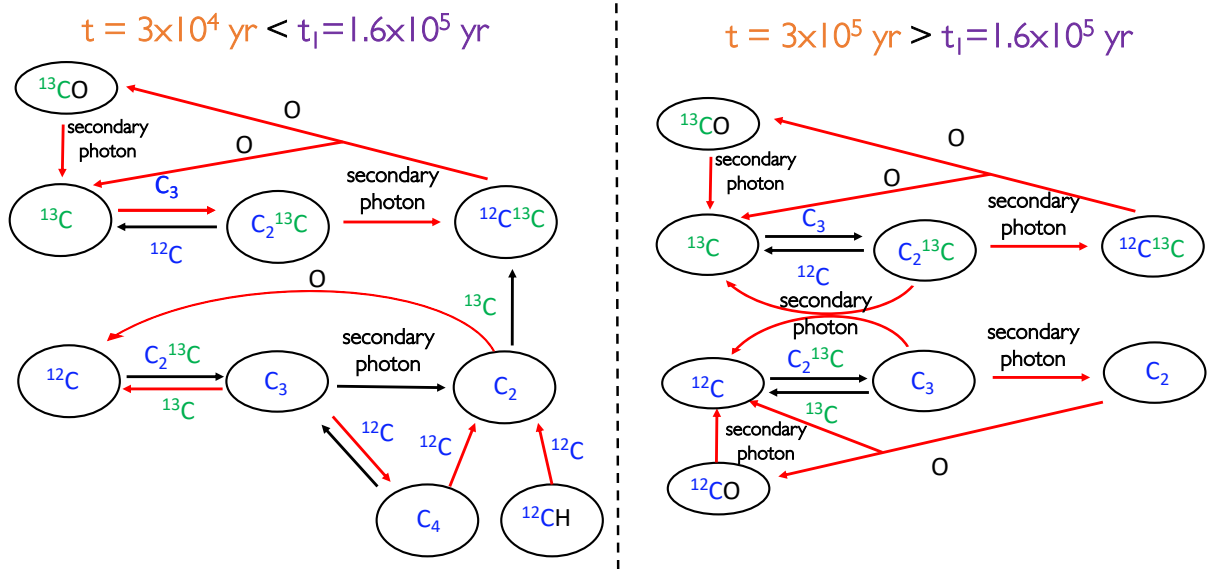


Fig. 4. Chemical pathways that distribute the two carbon isotopes in atomic carbon, C₂ and C₃ at 3×10^4 yr (*left panel*) and 3×10^5 yr (*right panel*), for the fiducial model. Main creation and destruction reactions are highlighted in red, ¹²C is represented in blue and ¹³C is represented in green.

Table 5. ¹²C/¹³C ratios for different molecules (C₃, C₂, C, CO, CN, HCN, and HNC) for three different times in the fiducial model: the early chemistry time (second row), t_1 , as defined in the text, and the times before and after t_1 that we have discussed in the text (first and third rows, respectively).

Time	¹² C/ ¹³ C						
	C ₃	C ₂	C	CO	CN	HCN	HNC
3×10^4 yr	6	68	163	35	50	88	106
$t_1 = 1.6 \times 10^5$ yr	7	24	211	63	65	68	76
3×10^5 yr	6	11	81	64	57	50	79

than the CN/¹³CN ratio, and it stays low for a longer time than that of CN (CN/¹³CN = 68 at t_1). Moreover, most of C₂ is formed

from atomic ¹²C through the cycle:



Conversely, C¹³C is mainly formed from ¹³CC₂ through secondary UV photon reactions². As a consequence, C₂/¹³CC ≈ 68 since it reaches an equilibrium between the efficient formation of C₂ from the very abundant ¹²C and the main formation of C¹³C from ¹³CC₂.

For $t > t_1$, the cycle of reactions (11) is not efficient any more since most of the atomic carbon has been transformed into CO. Thus, C₂ is mainly formed from C₃ reacting with secondary photons. C₂ then reacts with the remaining O, releasing

² The inner parts of a dense core are shielded from external UV photons, which can, in the inner regions, be created only through cosmic-ray-induced H₂ electronic excitation.

atomic carbon. At this time, the cycle of reactions described above is the same for ^{12}C and ^{13}C -containing species (red reactions in the right panel of Fig. 4). Since at this timescale the isotopic exchange reaction of C_3 is not efficient any more, the atomic $^{12}\text{C}/^{13}\text{C}$ ratio approaches the low values of C_3 . As a consequence, the $^{12}\text{C}/^{13}\text{C}$ ratio of carbon-chain and nitrile-bearing species, which are produced starting from atomic carbon, is low as well. This behaviour remains until the abundance of C_3 drops (when CO starts to freeze out on dust grains) and the $^{12}\text{C}/^{13}\text{C}$ ratios of the other molecular species rise again. When this happens, the main sink of ^{13}C is CO and, to a small extent, HCO^+ , and ^{13}C is diluted in all the other molecular species.

We would like to point out that in our chemical network, we did not introduce ^{13}C in reactions containing C_4 , as explained in Sect. 2.2, and some biases on C-fractionation of C_3 could arise because of this assumption. However, we found that the $\text{C}_4 + \text{O}$ reaction is not efficient for the formation of C_3 in our chemical network. Moreover, the radiative association of C_3 and C giving C_4 and the $\text{C}_4 + \text{C}$ reaction forming C_3 back, are much less efficient than the isotopic exchange reactions involving C_3 with our assumed reaction rate coefficients.

Recently, Giesen et al. (2020) reported the first detection of the ^{13}C -isotopologues of C_3 , ^{13}CCC and C^{13}CC , towards the massive star-forming region SgrB2(M), near the Galactic Centre. They derived an average $^{12}\text{C}/^{13}\text{C}$ abundance ratio of 20.5 ± 4.2 , in agreement with the value of 20 as derived from the galactocentric trend by Milam et al. (2005) for CN, CO, and H_2CO , taking into account the three molecules (Eq. (4)). Thus, it seems that no ^{13}C -fractionation for C_3 is detected in SgrB2, contrary to our fiducial model predictions. However, this chemical model is not appropriate to model the physical conditions and the chemistry towards this source. Furthermore, other observational studies towards the Galactic Centre are needed to improve the reliability of the $^{12}\text{C}/^{13}\text{C}$ estimated from the galactocentric trend. Finally, the authors found a $\text{N}(^{13}\text{CCC})/\text{N}(\text{C}^{13}\text{CC})$ ratio of 1.2 ± 0.1 , different from the statistically expected value³ (2). This discrepancy could be explained by a difference of 16 K in zero-point energy between the two species with respect to the main species C_3 , as shown in Table 2. The different position of the ^{13}C in carbon chains would probably lead to a higher abundance of C^{13}CC with respect to ^{13}CCC for $27 \text{ K} < T < 43 \text{ K}$ because of the reaction $\text{C}_3 + ^{13}\text{C} \rightarrow \text{C}^{13}\text{CC} + \text{C} + 43 \text{ K}$. Another difference is that the symmetry factor f for the reaction $\text{C}_3 + ^{13}\text{C} \rightarrow \text{C}^{13}\text{CC} + \text{C}$ is 1, while it is 2 for the reaction $\text{C}_3 + ^{13}\text{C} \rightarrow ^{13}\text{CCC} + \text{C}$. We plan to upgrade our chemical network to track the position of ^{13}C in molecules and hence to study the possible roles of the different ZPEs.

3.2. Parameter-space exploration

In this section, we focus the analysis on the nitrile-bearing species CN, HCN, and HNC in order to evaluate how reliable the estimates of the $^{14}\text{N}/^{15}\text{N}$ ratio based on $^{12}\text{C}/^{13}\text{C} = 68$ (Colzi et al. 2018a,b) are.

We analysed the $^{12}\text{C}/^{13}\text{C}$ ratio for different temperatures and densities in three well-defined fixed times: the early chemistry time t_1 , $t_2 = 2 \times t_1$, and $t_3 = 10 \times t_1$. The densities we analysed are between $2 \times 10^3 \text{ cm}^{-3}$ and $2 \times 10^7 \text{ cm}^{-3}$, and the temperatures are 10, 20, 30, 40, and 50 K. Figures 5–7 show the behaviour

³ Assuming a statistical distribution of ^{13}C in C_3 , there are two options to place it at the ends of the carbon chain and only one at the centre of the molecule.

of $\text{HN}^{12}\text{C}/\text{HN}^{13}\text{C}$, $\text{H}^{12}\text{CN}/\text{H}^{13}\text{CN}$, and $^{12}\text{CN}/^{13}\text{CN}$, respectively, as a function of n_{H} and for different temperatures. In particular, it can be noted that for t_1 and t_2 and for densities higher than 10^6 cm^{-3} , the $^{12}\text{C}/^{13}\text{C}$ ratios tend to be higher for 10 K with respect to higher temperatures. This is because the forward reaction (2) is efficient until $T < 17.4 \text{ K}$, together with the low-temperature isotopic exchange reaction for C_3 . Then, most of the ^{13}C is in CO, HCO^+ , and in C_3 .

It should be noted that this trend is also different depending on the density. This is because of the definition of t_1 : for a density of 10^6 cm^{-3} , t_1 is the time just before reaching the dip of carbon isotopic ratios that directly follows C_3 , while for a density of 10^5 cm^{-3} , t_1 is the time when the dip in $^{12}\text{C}/^{13}\text{C}$ is present and follows that of C_3 . The higher the density, the later the dip of lower $^{12}\text{C}/^{13}\text{C}$ with respect to t_1 when most of the atomic C is in the form of CO. The most probable explanation, also following what was described in Sect. 3.1.3, is that there is a competition between the O atoms transformed into CO and frozen out on grains, and those that are still available to take part in the reactions shown in the right panel of Fig. 4.

Overall, for densities of $\sim 10^3\text{--}10^4 \text{ cm}^{-3}$, the $^{12}\text{C}/^{13}\text{C}$ ratio is almost always higher than the canonical value of 68. Moreover, for a density $\approx 10^5 \text{ cm}^{-3}$, the $^{12}\text{C}/^{13}\text{C}$ ratio is consistent with 68 within a factor two, except for HCN and HNC for temperatures below 20 K at t_1 and t_3 .

We also performed the same parameter-space exploration for CO, HCO^+ , and H_2CO , to also show the predicted $^{12}\text{C}/^{13}\text{C}$ ratios for these molecular species (see Appendix B).

3.2.1. Low-mass star-forming regions

As already discussed in the introduction of this chapter, Daniel et al. (2013) found $\text{HNC}/\text{HN}^{13}\text{C} = 20_{-4}^{+5}$, $\text{HCN}/\text{H}^{13}\text{CN} = 30_{-4}^{+7}$, and $\text{CN}/^{13}\text{CN} = 50_{-11}^{+19}$ towards B1b, and Magalhães et al. (2018) obtained a $\text{HCN}/\text{H}^{13}\text{CN}$ ratio of 45 ± 3 towards the pre-stellar core L1498. Daniel et al. (2013) derived a hydrogen density of $6 \times 10^6 \text{ cm}^{-3}$ and a temperature of 17 K towards the centre of the pre-stellar core. Furthermore, Magalhães et al. (2018) found, for the centre of the core, an average hydrogen density of $2 \times 10^5 \text{ cm}^{-3}$ and a temperature of 10 K. Thus, we used these physical properties to study the $^{12}\text{C}/^{13}\text{C}$ ratios predicted by our chemical model. The comparison is shown in Figs. 5–7.

For CN, we reproduced the values observed by Daniel et al. (2013) at time t_3 , while for HCN and HNC, the values we found with our model are slightly higher. We note that the results of Daniel et al. (2013) for HCN and HNC have large error bars because the HCN and HNC lines are heavily saturated. Opacity effects strongly impact the column density derivations and may lead to an underestimation of the main isotope column density, and thus of the $^{12}\text{C}/^{13}\text{C}$ ratios. This could explain why we are not able to reproduce the values derived by Daniel et al. (2013). Moreover, we can reproduce the value observed for HCN by Magalhães et al. (2018) at time t_2 . This behaviour is also shown in Fig. 8, which represents the time evolution of the $^{12}\text{C}/^{13}\text{C}$ ratio for the two models corresponding to the two observed low-mass star-forming regions. We note that since the model is not simulating dynamical evolution, the fact that different observations could be reproduced at different times cannot be used to conclude anything about the chemical age of the simulated star-forming region. In addition, we remind the reader that the initial conditions were taken somewhat arbitrarily, so the displayed time dependence is only indicative.

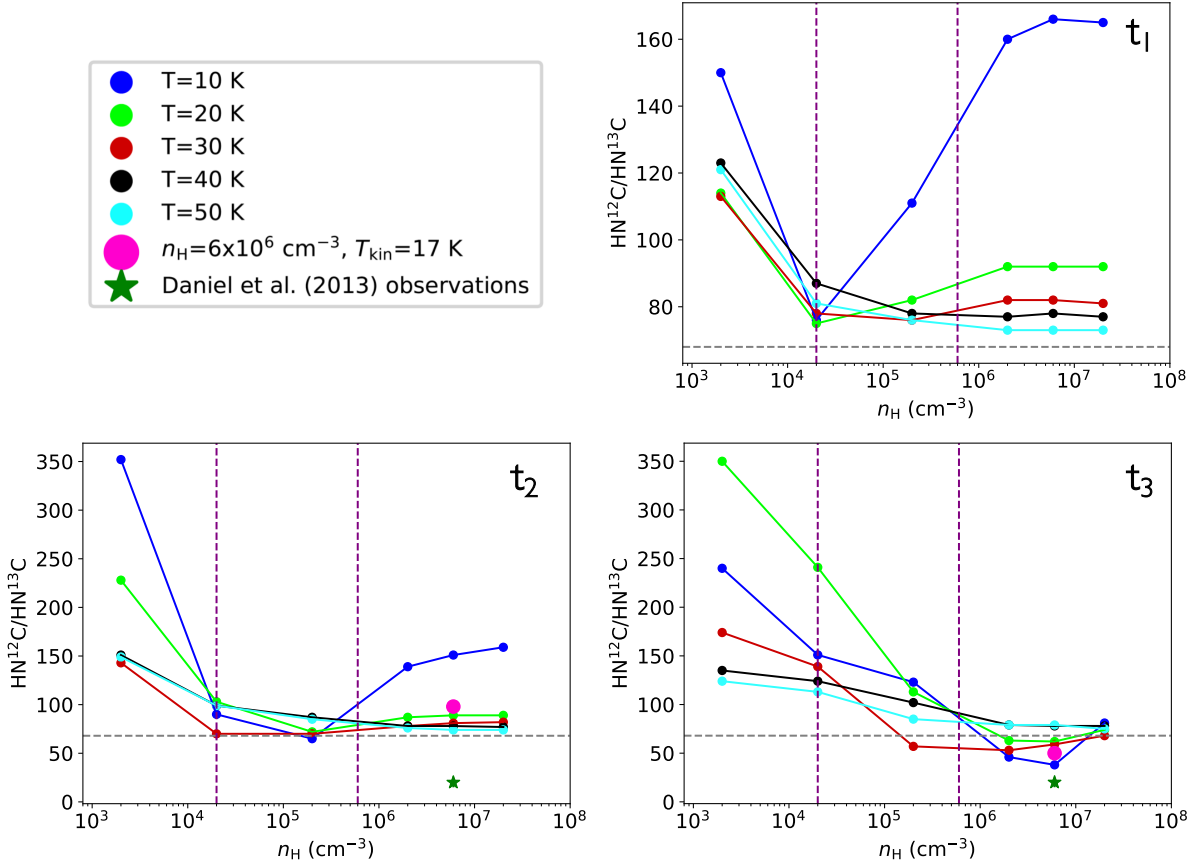


Fig. 5. $\text{HN}^{12}\text{C}/\text{HN}^{13}\text{C}$ ratio as a function of n_{H} , for different temperatures, at t_1 (top right panel), t_2 (bottom left panel), and t_3 (bottom right panel). The large pink circles in the bottom panels represent the result of the model that simulates the physical conditions in the centre of the pre-stellar core B1b observed by Daniel et al. (2013). The $\text{HN}^{12}\text{C}/\text{HN}^{13}\text{C}$ ratio observed by Daniel et al. (2013) is represented by the dark green star. We note that the error bar is within the symbol. In all the panels, the two vertical purple dashed lines represent the range of densities of the sample of high-mass star-forming region described in Sect. 3.2.2, and the black horizontal dashed lines represent the initial $^{12}\text{C}/^{13}\text{C}$ ratio of 68.

3.2.2. High-mass star-forming regions sample

We used our model grid to estimate the $^{12}\text{C}/^{13}\text{C}$ ratio for HNC and HCN towards the sample of high-mass star-forming regions observed by Colzi et al. (2018a). In particular, we used the H_2 column densities listed in Table 1 by Fontani et al. (2018) to derive the H_2 densities towards the region described by the SCUBA or APEX effective beam⁴. The average n_{H} of the sources ranges from $2 \times 10^4 \text{ cm}^{-3}$ up to $6 \times 10^5 \text{ cm}^{-3}$. The kinetic temperatures, given in Table 3 of Colzi et al. (2018a), are in between 14 and 47 K, and are similar to the range of values used in the grid of models performed earlier in this section. With this information, we can constrain the $^{12}\text{C}/^{13}\text{C}$ ratios predicted by our models that could be used to compute N-fractionation from ^{13}C -isotopologue observations. Figures 5 and 6 show the $\text{HN}^{12}\text{C}/\text{HN}^{13}\text{C}$ and $\text{H}^{12}\text{CN}/\text{H}^{13}\text{CN}$ ratios for the three analysed times, together with the observed volume-density range.

The $^{12}\text{C}/^{13}\text{C}$ ratios derived for t_1 , t_2 , and t_3 , and the errors made when the $^{14}\text{N}/^{15}\text{N}$ ratios are measured assuming a fixed local $^{12}\text{C}/^{13}\text{C}$ ratio of 68, for HNC and HCN, are listed in Table 6. Taking, for example, one of the sources with the highest H_2 number density, 19 410+2336, with $n_{\text{H}} = 5.8 \times 10^5 \text{ cm}^{-3}$ and $T_{\text{gas}} = 21 \text{ K}$, Colzi et al. (2018a) derived a $\text{HNC}/\text{H}^{15}\text{NC}$ ratio of 431 ± 24 . For the early chemistry time, we obtain

⁴ The effective beam of the continuum observations is $22''$ for SCUBA and $15''$ for APEX. The instrument used for each source is given in Table 1 of Fontani et al. (2018).

Table 6. $^{12}\text{C}/^{13}\text{C}$ ratios predicted for HNC and HCN in the range of temperatures and densities of the high-mass star-forming regions sample observed by Colzi et al. (2018a) (Cols. 2 and 3).

Time	$R_1 = \frac{\text{HN}^{12}\text{C}}{\text{HN}^{13}\text{C}}$	$R_2 = \frac{\text{H}^{12}\text{CN}}{\text{H}^{13}\text{CN}}$	$R_1/68$	$R_2/68$
t_1	74–135	68–121	1.1–1.9	1–1.8
t_2	68–97	52–96	1–1.4	0.8–1.4
t_3	53–240	52–210	0.8–3.5	0.8–3.1

Notes. The fourth and fifth columns present the error factor made when deriving $^{14}\text{N}/^{15}\text{N}$ ratios assuming a local $^{12}\text{C}/^{13}\text{C}$ ratio of 68.

$\text{HNC}/\text{H}^{15}\text{NC} \sim 550$. For t_2 it is ~ 495 , and for t_3 the ratio goes down to ~ 370 . This shows that our results are time-dependent, thus care needs to be taken in the comparison with observations, because the chemical times may not correspond to the dynamical age of the star-forming region. So, a more accurate model including also the evolution of physical parameters is necessary to better constrain the timescales. Moreover, the H_2 column densities are derived from regions ($15''$ or $22''$) that probably also include the more diffuse gas that surrounds the denser cores in which star formation occurs. As an example, Beuther et al. (2007) derived an H_2 column density of $\sim 10^{23}\text{--}10^{24} \text{ cm}^{-2}$ in regions of $\sim 2''$ in size towards the denser cores of the high-mass protocluster IRAS 05358 (see also

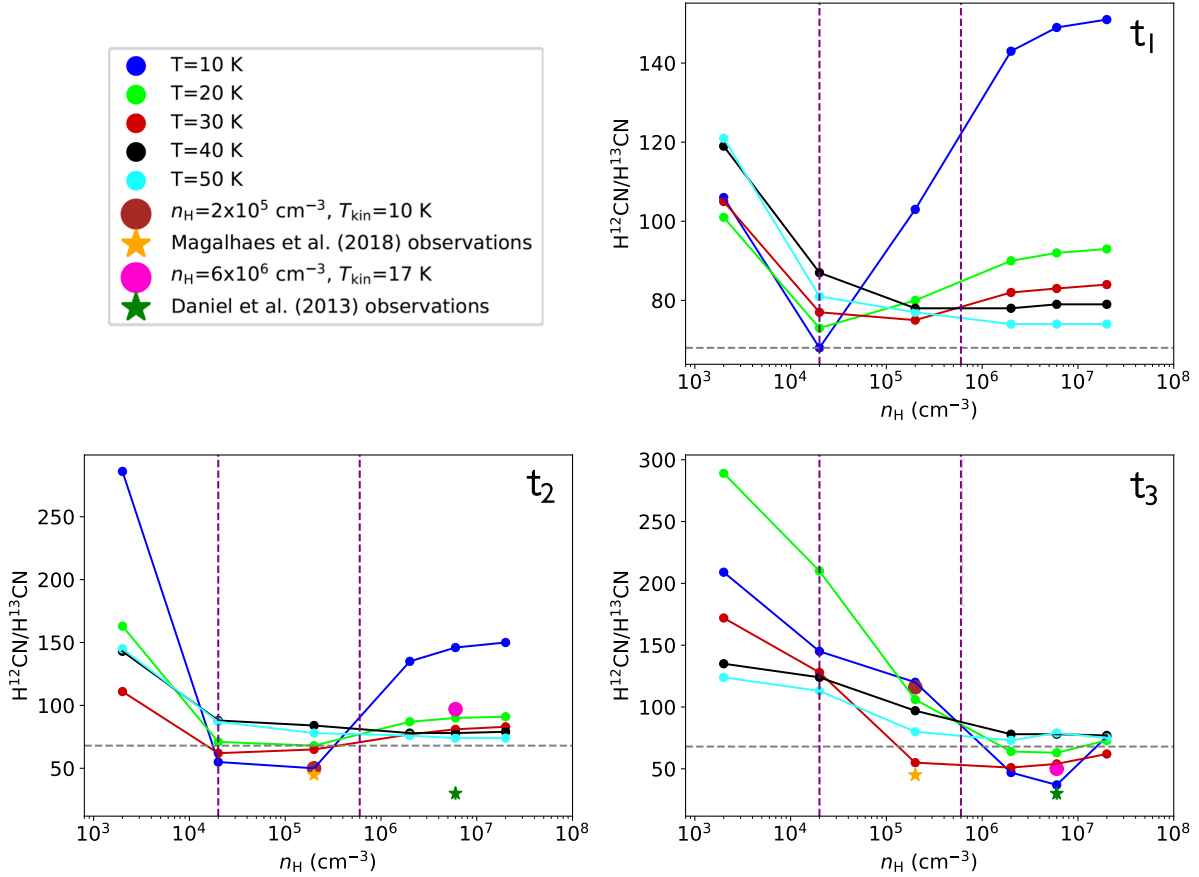


Fig. 6. $\text{H}^{12}\text{CN}/\text{H}^{13}\text{CN}$ ratio as a function of n_{H} , for different temperatures, at t_1 (top right panel), t_2 (bottom left panel), and t_3 (bottom right panel). The large pink and brown circles in the bottom panels represent the result of the model that simulates the physical conditions in the centre of the pre-stellar cores B1b observed by Daniel et al. (2013) and L1498 observed by Magalhães et al. (2018), respectively. The $\text{H}^{12}\text{CN}/\text{H}^{13}\text{CN}$ ratios observed by Daniel et al. (2013) and Magalhães et al. (2018) are represented by the dark green and orange stars, respectively. We note that the error bars are within the symbols. In all panels, the two vertical purple dashed lines represent the range of densities of the sample of high-mass star-forming region described in Sect. 3.2.2, and the black horizontal dashed lines represent the initial $^{12}\text{C}/^{13}\text{C}$ ratio of 68.

Colzi et al. 2019). These column densities correspond to H_2 number densities of $\sim 10^6\text{--}10^7\text{ cm}^{-3}$ that are one or two orders of magnitude higher than those used in this section to compare with the model. Thus, detailed continuum observations and a description of the structures of these regions are needed.

3.2.3. Effect of cosmic rays

Finally, we discuss the possible effect of different cosmic-ray ionisation rates (ζ) in the fiducial model. Until now, we used the canonical value of $1.3 \times 10^{-17}\text{ s}^{-1}$ (e.g. Padovani et al. 2009). We analyse here how the main formation and destruction routes (cf. Fig. 4) change when one assumes lower and higher ζ with respect to the standard one: $\zeta_{\text{low}} = 1.3 \times 10^{-18}\text{ s}^{-1}$ and $\zeta_{\text{high}} = 1.3 \times 10^{-16}\text{ s}^{-1}$, respectively. For example, ζ_{high} is similar to the value derived in the diffuse cloud in the vicinity of OMC-2 FIR4 by López-Sepulcre et al. (2013) ($2.3 \times \zeta_{\text{high}}$), and Caselli et al. (1998) used deuterium fraction measurements of HCO^+ to constrain ζ in the range of $10^{-18}\text{--}10^{-16}\text{ s}^{-1}$ towards 24 cloud cores.

In the case of ζ_{low} , the early chemistry time is 1.9×10^5 yr, and in the model with ζ_{high} it is reduced to 5.8×10^4 yr. Figures 9 and 10 show the behaviour of the abundances and $^{12}\text{C}/^{13}\text{C}$ ratios of the same molecules studied for the fiducial model, for ζ_{low} and ζ_{high} , respectively. For these two models, we studied in

detail two time-scales, before and after the early chemistry time. Figures C.1 and C.2 represent the main destruction and formation pathways of various species for ζ_{low} and ζ_{high} , respectively.

In the case of ζ_{low} , for $t < t_1$, ^{12}C is very abundant, as in the standard case, because of the efficiency of the low-temperature isotopic exchange reactions. However, in this model the $\text{C}_2/\text{C}^{13}\text{C}$ ratio is also higher than 68 and similar to the C-fractionation of atomic carbon. In fact, the secondary photon reactions are less efficient in creating C^{13}C starting from C_2^{13}C . For $t > t_1$, the isotopic exchange reaction involving C_3 is still efficient since the destruction reaction of C_2^{13}C with secondary photons is not as significant as in the fiducial model. However, the atomic $^{12}\text{C}/^{13}\text{C}$ ratio decreases with the depletion of ^{12}C onto grain surfaces. Moreover, the abundances of atomic carbon and related molecules (like C_3 and CN) do not increase again in the late chemistry since He^+ is not efficiently produced by cosmic-ray reactions, owing to the low ζ . This also affects the decrease of the $^{12}\text{C}/^{13}\text{C}$ ratios.

In the case of ζ_{high} , for $t < t_1$, reactions with secondary photons are the most important ones. Thus, both ^{12}C - and ^{13}C -containing species follow the same chemical pathway (see left panel of Fig. C.2). In this case, C_2 inherits the $^{12}\text{C}/^{13}\text{C}$ ratio from C_3 (which is lower than 68), and the C-fractionation of atomic carbon and C_3 is still governed by the very efficient low-temperature isotopic exchange reaction. For $t > t_1$, the behaviour

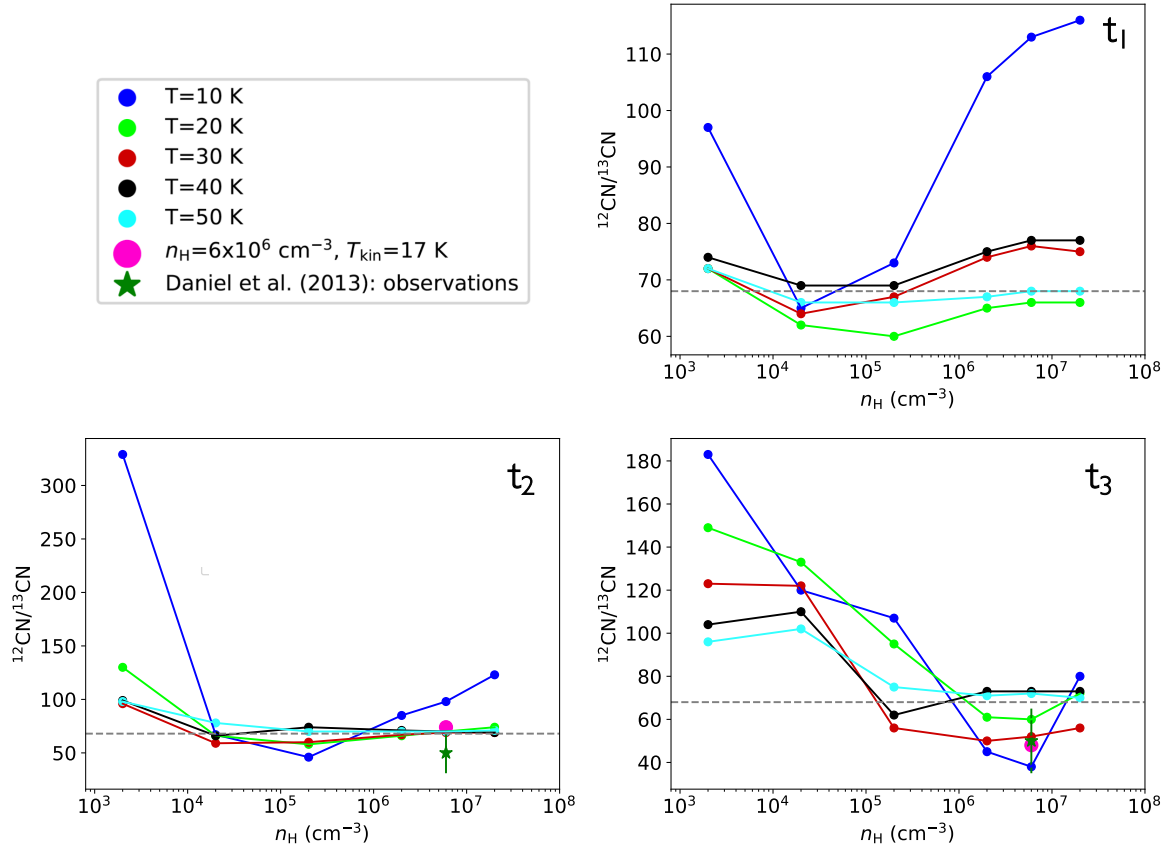


Fig. 7. $^{12}\text{CN}/^{13}\text{CN}$ ratio as a function of n_{H} , for different temperatures, at t_1 (top right panel), t_2 (bottom left panel), and t_3 (bottom right panel). The large pink circles in the bottom panels represent the result of the model that simulates the physical conditions in the centre of the pre-stellar core B1b observed by Daniel et al. (2013). The $^{12}\text{CN}/^{13}\text{CN}$ ratio observed by Daniel et al. (2013) is represented by the green star. We note that the error bar is within the symbol. In all panels, the black horizontal dashed line represents the initial $^{12}\text{C}/^{13}\text{C}$ ratio of 68.

is similar to that of the fiducial model. The main difference is that the isotopic exchange reaction of C_3 is still efficient since secondary photons create more atomic ^{13}C (from C_2 whose C-fractionation is inherited by C_3) than in the fiducial model, maintaining the efficiency of this reaction for longer. As a consequence, the atomic $^{12}\text{C}/^{13}\text{C}$ ratio remains higher and there is no decreasing trend towards values lower than 68, not even for the molecules related to atomic carbon (CN, HCN, HNC). In the late chemistry time, atomic carbon and C-chains form very efficiently because of the enhanced abundance of He^+ due to the higher cosmic-ray ionisation rate. This effect maintains a higher abundance of atomic carbon, and consequently the atomic $^{12}\text{C}/^{13}\text{C}$ ratio is larger.

We also performed a parameter-space exploration for a fixed n_{H} of $2 \times 10^4 \text{ cm}^{-3}$, varying the temperatures from 10 up to 50 K and the cosmic-ray ionisation rate between ζ_{low} and ζ_{high} . In particular, as already done in Sect. 3.2, we focused the analysis on HNC, HCN, and CN (Figs. 11–13). The main trend is that the $^{12}\text{C}/^{13}\text{C}$ ratios are highest for ζ_{high} . This is related to the fact that secondary photon reactions maintain a high efficiency of low-temperature isotopic exchange reactions that involve C_3 , and the atomic $^{12}\text{C}/^{13}\text{C}$ ratio (and that of related molecules) remains higher than 68 (see also Fig. C.2, right panel).

4. Conclusions

We developed a new chemical network to study, in detail, how important isotopic exchange reactions are to the chemistry of

carbon-containing species in the low temperature (10–50 K) gas in star-forming regions with $n_{\text{H}} = 2 \times 10^3 - 2 \times 10^7 \text{ cm}^{-3}$. In particular, we suggest the occurrence of ^{13}C exchange involving C_3 with atomic carbon and study the possible consequences of this reaction. The main results and conclusions of this work are summarised below:

1. We found that reaction (10) is mainly important for $T_{\text{gas}} < 27 \text{ K}$ (owing to its exothermicity), and leads to $^{12}\text{C}/^{13}\text{C} < 68$ for molecules that form from atomic carbon (e.g. C_2 , C_3 , and nitrile-bearing species). This behaviour occurs in the time period between the conversion of atomic carbon into CO, and the time when CO is almost completely frozen out onto dust grains.
2. We performed a detailed study of the $^{12}\text{C}/^{13}\text{C}$ ratios for the nitrile-bearing species HCN, HNC, and CN, as a function of density and for different temperatures. Our model can partially reproduce the carbon isotopic ratios derived by Daniel et al. (2013) and Magalhães et al. (2018) from observations towards low-mass pre-stellar cores.
3. We also used our grid of models to evaluate how far we are from the correct $^{12}\text{C}/^{13}\text{C}$ ratio, assumed to be 68 in the local ISM, to derive the $^{14}\text{N}/^{15}\text{N}$ ratios in the sample of high-mass star-forming regions analysed by Colzi et al. (2018a). Our chemical model predicts that we are overestimating or underestimating the assumed $^{12}\text{C}/^{13}\text{C}$ ratios by factors ~ 0.8 – 1.9 , even up to ~ 3.5 , depending on the evolutionary time that we choose for the analysis. Considering these factors, the average nitrogen fractionation value of ~ 330 derived by

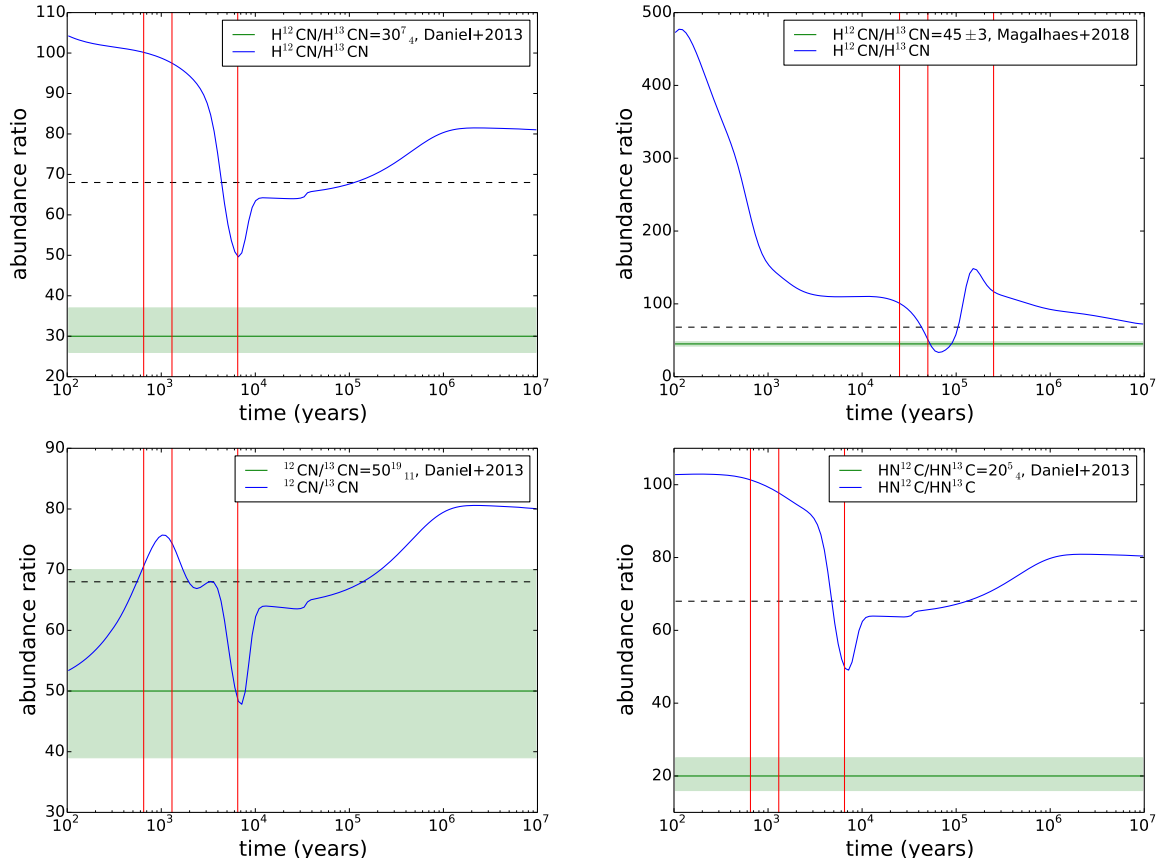


Fig. 8. *Top-right panel:* time evolution of the $^{12}\text{C}/^{13}\text{C}$ ratio for HCN for the model that simulates the centre of the pre-stellar core L1498 observed by Magalhães et al. (2018) ($n_{\text{H}} = 2 \times 10^5 \text{ cm}^{-3}$ and $T_{\text{gas}} = 10 \text{ K}$). *Top-left panel and bottom panels:* time evolution of the $^{12}\text{C}/^{13}\text{C}$ ratio for HCN, CN, and HNC for the model that simulates the centre of the pre-stellar core B1b observed by Daniel et al. (2013) ($n_{\text{H}} = 6 \times 10^6 \text{ cm}^{-3}$ and $T_{\text{gas}} = 17 \text{ K}$). In all panels, the green horizontal line indicates the observed ratio, with the associated uncertainty as a green area. The three red vertical lines represent t_1 , t_2 , and t_3 . The black horizontal dashed line represents the initial $^{12}\text{C}/^{13}\text{C}$ ratio of 68.

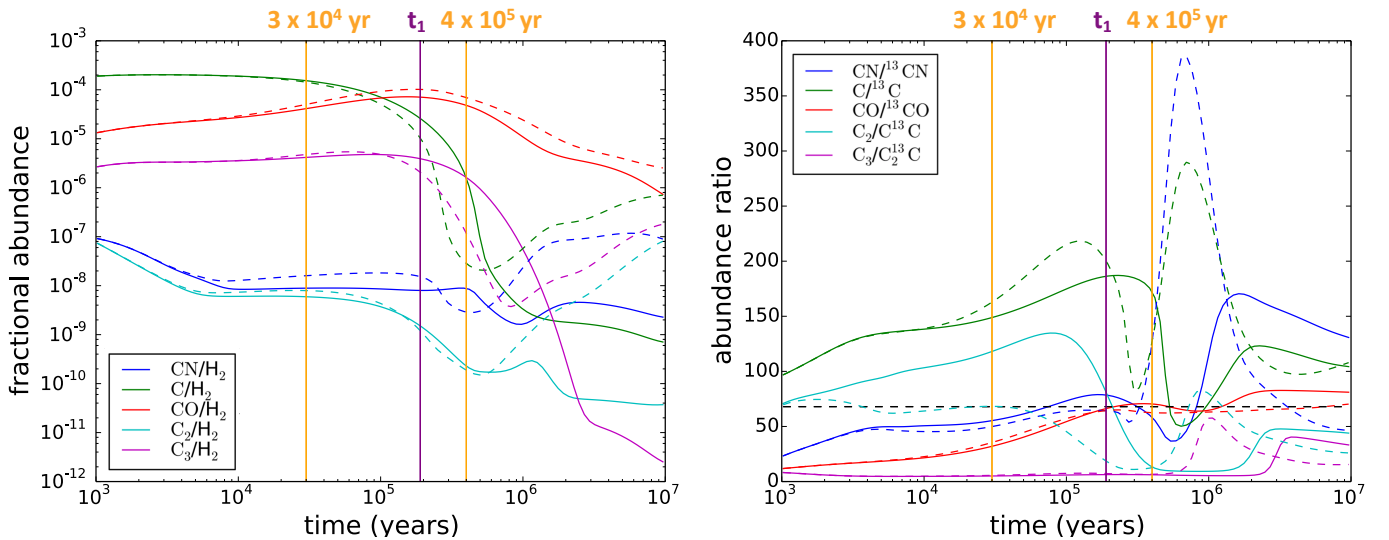


Fig. 9. *Left panel:* time evolution of CN, C, CO, C_2 , and C_3 abundances with respect to H_2 for the fiducial model with a cosmic-ray ionisation rate of $1.3 \times 10^{-18} \text{ s}^{-1}$. *Right panel:* time evolution of the $^{12}\text{C}/^{13}\text{C}$ ratio for CN, C, CO, C_2 , and C_3 for the fiducial model with a cosmic-ray ionisation rate of $1.3 \times 10^{-18} \text{ s}^{-1}$. In both panels, the vertical purple solid line represents the early chemistry time as defined in the text, while the two vertical orange solid lines represent the two times ($3 \times 10^4 \text{ yr}$, and $4 \times 10^5 \text{ yr}$) that we have analysed and discussed in the text. The trends obtained with the standard ζ of the fiducial model are superimposed with dashed lines. The black horizontal dashed line represents the initial $^{12}\text{C}/^{13}\text{C}$ ratio of 68.

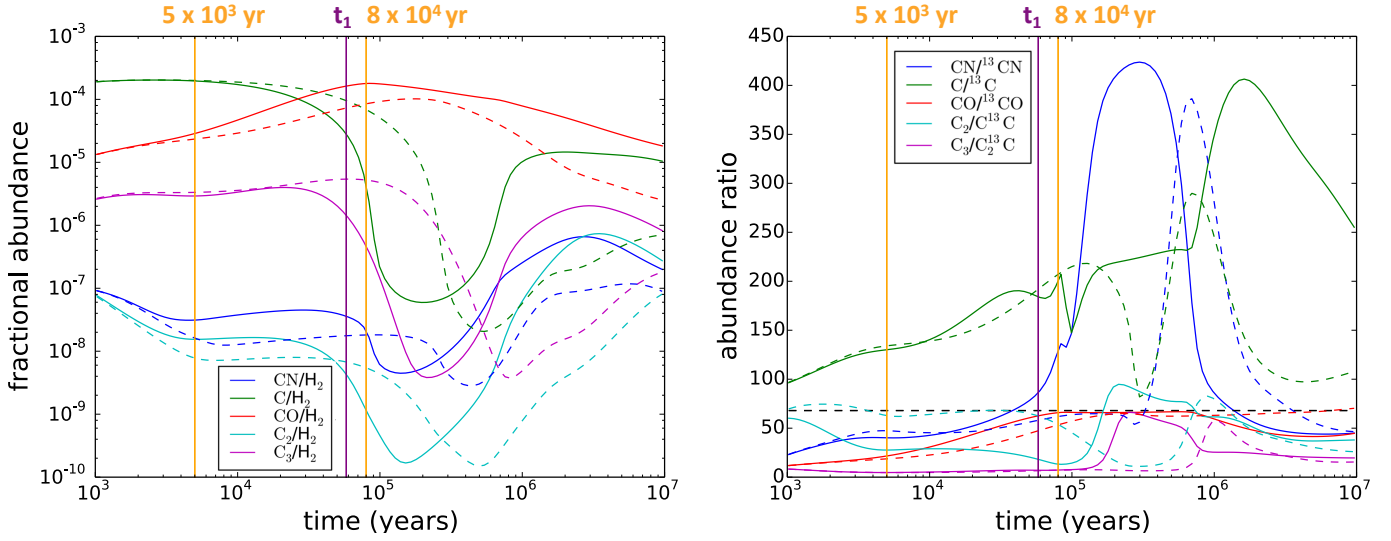


Fig. 10. Left panel: same as Fig. 9, but for $\zeta = 1.3 \times 10^{-16} \text{ s}^{-1}$. In both panels, the vertical purple solid line represents the early chemistry time as defined in the text, while the two vertical orange solid lines represent the two times ($5 \times 10^3 \text{ yr}$, and $8 \times 10^4 \text{ yr}$) that we analyse and discuss in the text. The trends obtained with the standard ζ of the fiducial model are superimposed with dashed lines. The black horizontal dashed line represent the initial $^{12}\text{C}/^{13}\text{C}$ ratio of 68.

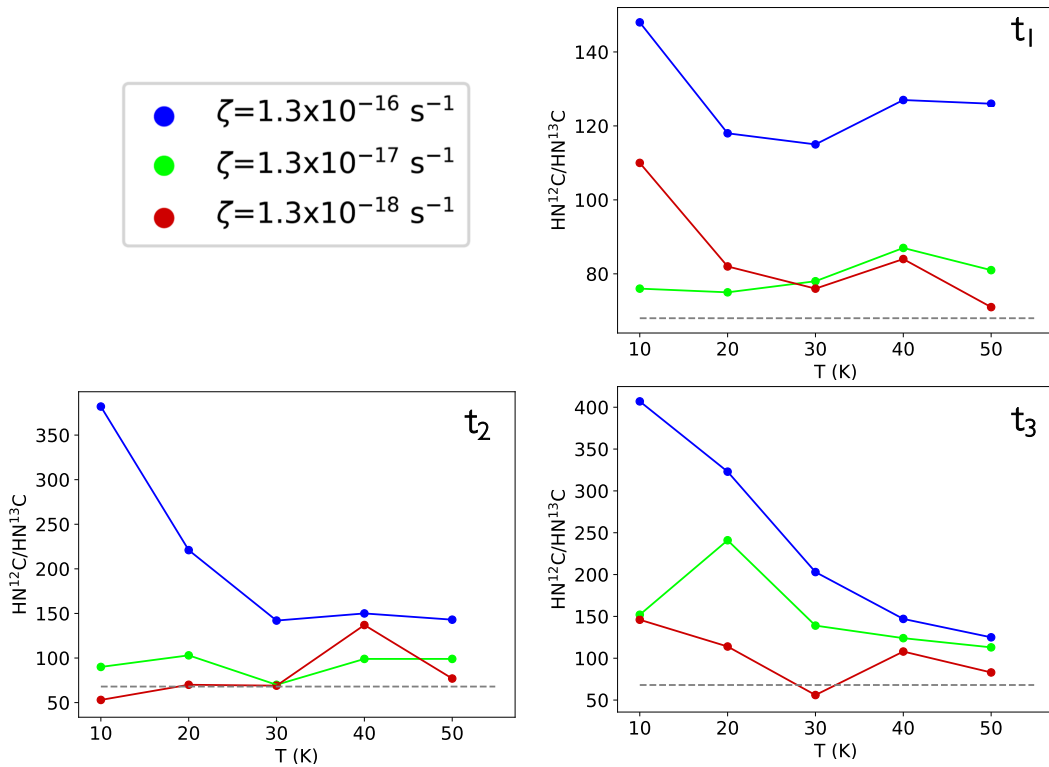


Fig. 11. $\text{HN}^{12}\text{C}/\text{HN}^{13}\text{C}$ ratio as a function of the temperature, for different cosmic-ray ionisation rates, at t_1 (top-right panel), t_2 (bottom-left panel), and t_3 (bottom-right panel). The black horizontal dashed line represents the initial $^{12}\text{C}/^{13}\text{C}$ ratio of 68.

Colzi et al. (2018a) and Colzi et al. (2018b) for HCN and HNC, could become 260–1150. This range would include both the low values measured in comets (e.g. 250), and the higher values found in low-mass pre-stellar cores (e.g. ~ 630 –770 for N_2H^+ by Redaelli et al. 2018). This highlights the importance of knowing the precise $^{12}\text{C}/^{13}\text{C}$ ratios in studies of nitrogen fractionation with the double-isotope method.

4. Finally, we performed a parameter-space exploration of the $^{12}\text{C}/^{13}\text{C}$ ratios for nitrile-bearing species, varying the

cosmic-ray ionisation rate (ζ). We found that for ζ higher than the standard value of $1.3 \times 10^{-17} \text{ s}^{-1}$, the $^{12}\text{C}/^{13}\text{C}$ ratios are on average higher than in the cases with lower ζ . This result is due to the importance of secondary photon reactions in maintaining the efficiency of the isotopic exchange reactions involving C_3 , and to cosmic rays, which lead to an efficient production of atomic carbon and C-chains.

In a future work, we will upgrade the chemical network to cover nitrogen fractionation as well. This way, we will be able to

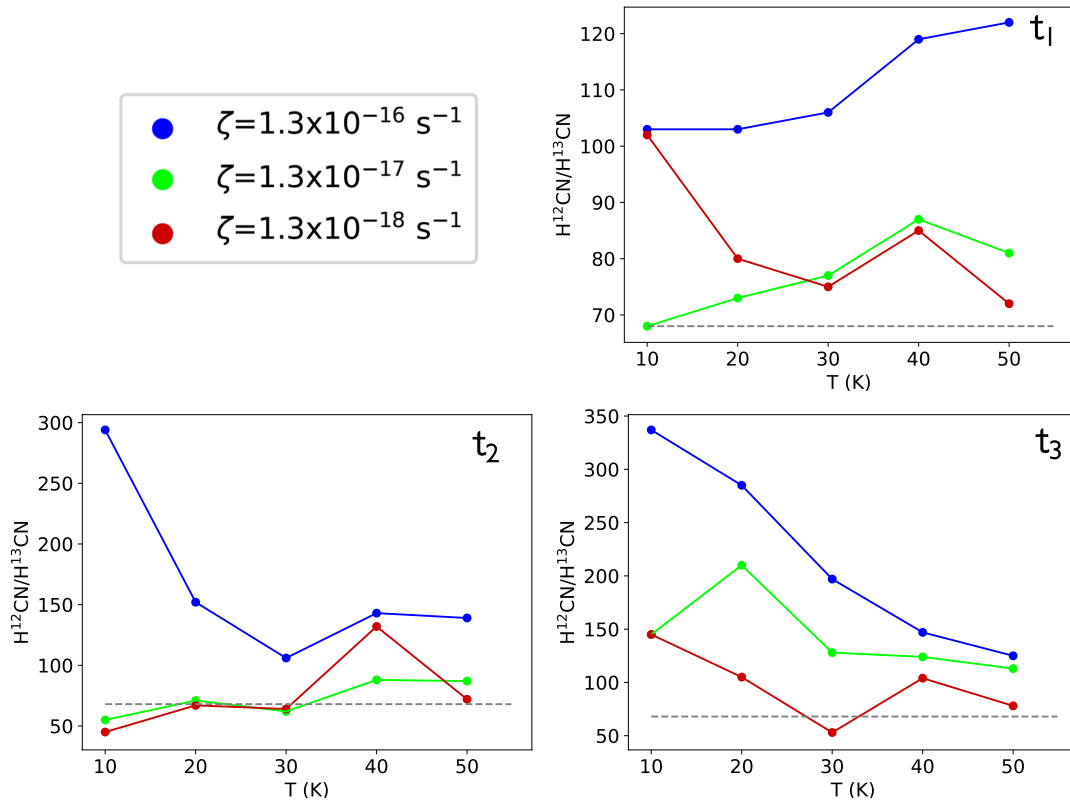


Fig. 12. Same as Fig. 11, but for $H^{12}CN/H^{13}CN$.

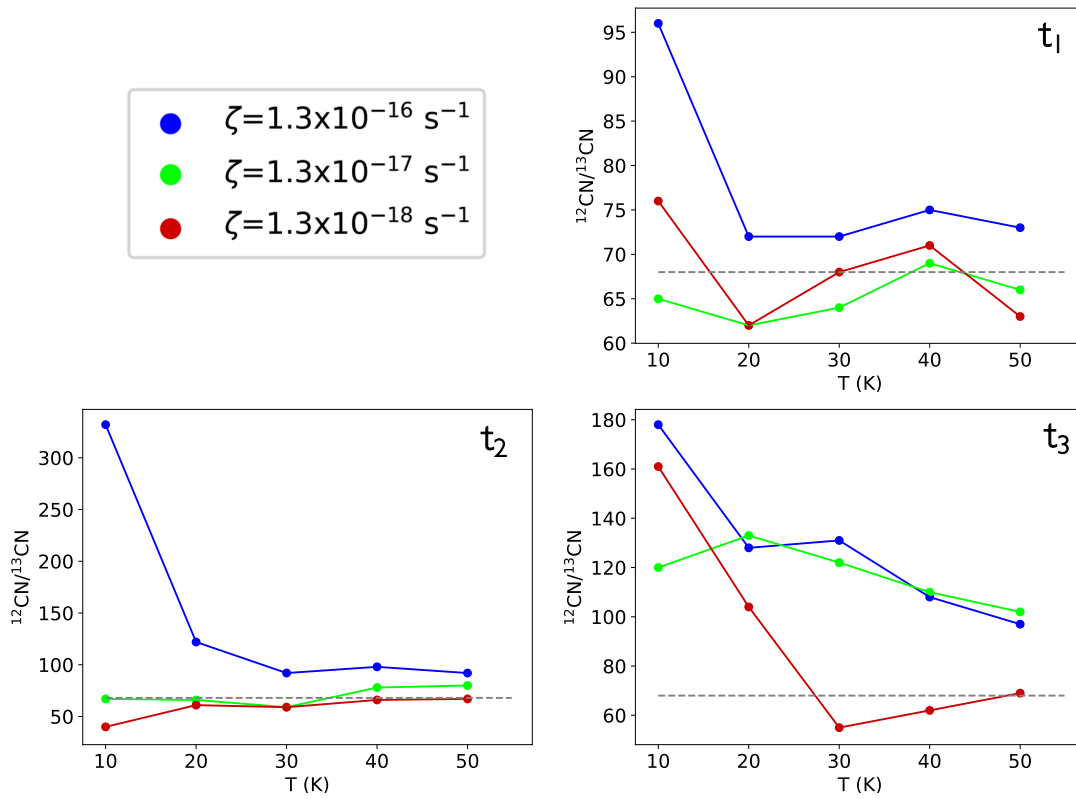


Fig. 13. Same as Fig. 11, but for $^{12}CN/^{13}CN$.

better describe the interplay between carbon and nitrogen isotope chemistry. The inclusion of the position of ^{13}C in multiple carbon bearing species is also another challenge left for future work.

Acknowledgements. Many thanks to the anonymous referee for the careful reading of the paper and the comments that improved the work. This publication has received funding from the European Union's Horizon 2020 research and innovation programme under grant agreement No 730562 [RadioNet]. L.C. acknowledges support from the Italian Ministero dell'Istruzione, Università e Ricerca through the grant Progetti Premiali 2012 – iALMA (CUP C52I13000140001). PC acknowledges support from the European Research Council (project PALs 320620). E.R. acknowledges partial support by the “Physique et Chimie du Milieu Interstellaire” (PCMI) of CNRS/INSU with INC/INP co-funded by CEA and CNES. Most of the figures were generated with the PYTHON-based package MATPLOTLIB (Hunter 2007).

References

- Ádámkóvics, M., Blake, G. A., & McCall, B. J. 2003, *ApJ*, **595**, 235
- Bergeman, T., & Cossart, D. 1981, *J. Mol. Spectr.*, **87**, 119
- Beuther, H., Leurini, S., Schilke, P., et al. 2007, *A&A*, **466**, 1065
- Boehle, A., Ghez, A. M., Schödel, R., et al. 2016, *ApJ*, **830**, 17
- Caselli, P., & Ceccarelli, C. 2012, *A&ARv*, **20**, 56
- Caselli, P., Walmsley, C. M., Terzieva, R., & Herbst, E. 1998, *ApJ*, **499**, 234
- Ceccarelli, C., Caselli, P., Bockelée-Morvan, D., et al. 2014, in *Protostars and Planets VI*, eds. H. Beuther, R. S. Klessen, C. P. Dullemond, & T. Henning (Tucson: University of Arizona Press), 859
- Colzi, L., Fontani, F., Caselli, P., et al. 2018a, *A&A*, **609**, A129
- Colzi, L., Fontani, F., Rivilla, V. M., et al. 2018b, *MNRAS*, **478**, 3693
- Colzi, L., Fontani, F., Caselli, P., et al. 2019, *MNRAS*, **485**, 5543
- Daniel, F., Gérin, M., Roueff, E., et al. 2013, *A&A*, **560**, A3
- Fontani, F., Caselli, P., Palau, A., Bizzocchi, L., & Ceccarelli, C. 2015, *ApJ*, **808**, L46
- Fontani, F., Vagnoli, A., Padovani, M., et al. 2018, *MNRAS*, **481**, 79
- Fontani, F., Quaiá, G., Ceccarelli, C., et al. 2020, *MNRAS*, **493**, 3412
- Furuya, K., Aikawa, Y., Sakai, N., & Yamamoto, S. 2011, *ApJ*, **731**, 38
- Galazutdinov, G., Pétlewski, A., Musaev, F., et al. 2002, *A&A*, **395**, 969
- Giesen, T. F., Mookerjee, B., Fuchs, G. W., et al. 2020, *A&A*, **633**, A120
- Haffner, L. M., & Meyer, D. M. 1995, *ApJ*, **453**, 450
- Hennig, P., Kraemer, W. P., & Dierksen, G. H. F. 1977, A compilation of theoretical spectroscopic constants and rotational-vibrational transition frequencies for the isoelectronic series of linear triatomic molecules HCN, HNC, HCO+, HOC+, HNN+ obtained from ab initio calculated energy hypersurfaces, Internal Report, MPI/PAE Astro 135, Max-Planck Institut, München
- Hily-Blant, P., Bonal, L., Faure, A., & Quirico, E. 2013a, *Icarus*, **223**, 582
- Hily-Blant, P., Pineau des Forêts, G., Faure, A., Le Gal, R., & Padovani, M. 2013b, *A&A*, **557**, A65
- Huber, K., & Herzberg, G. 1979, *Molecular Spectra and Molecular Structure – IV. Constants of Diatomic Molecules* (New York: Van nostrand Reinhold company)
- Hunt, J. A. S., Bovy, J., & Carlberg, R. G. 2016, *ApJ*, **832**, L25
- Hunter, J. D. 2007, *Comput. Sci. Eng.*, **9**, 90
- Langer, W. D., & Penzias, A. A. 1990, *ApJ*, **357**, 477
- Langer, W. D., & Penzias, A. A. 1993, *ApJ*, **408**, 539
- Langer, W. D., Wilson, R. W., Henry, P. S., & Guelin, M. 1978, *ApJ*, **225**, L139
- Langer, W. D., Graedel, T. E., Frerking, M. A., & Armentrout, P. B. 1984, *ApJ*, **277**, 581
- Le Petit, F., Roueff, E., & Le Bourlot, J. 2002, *A&A*, **390**, 369
- López-Sepulcre, A., Kama, M., Ceccarelli, C., et al. 2013, *A&A*, **549**, A114
- Magalhães, V. S., Hily-Blant, P., Faure, A., Hernandez-Vera, M., & Lique, F. 2018, *A&A*, **615**, A52
- Maier, J. P., Lakin, N. M., Walker, G. A. H., & Bohlender, D. A. 2001, *ApJ*, **553**, 267
- Milam, S. N., Savage, C., Brewster, M. A., Ziurys, L. M., & Wyckoff, S. 2005, *ApJ*, **634**, 1126
- Mladenović, M., & Roueff, E. 2014, *A&A*, **566**, A144
- Mookerjee, B., Hassel, G. E., Gerin, M., et al. 2012, *A&A*, **546**, A75
- Mookerjee, B., Vastel, C., Hassel, G. E., et al. 2014, *A&A*, **566**, A61
- Oka, T., Thorburn, J. A., McCall, B. J., et al. 2003, *ApJ*, **582**, 823
- Padovani, M., Galli, D., & Glassgold, A. E. 2009, *A&A*, **501**, 619
- Redaelli, E., Bizzocchi, L., Caselli, P., et al. 2018, *A&A*, **617**, A7
- Röllig, M., & Ossenkopf, V. 2013, *A&A*, **550**, A56
- Romano, D., Matteucci, F., Zhang, Z. Y., Papadopoulos, P. P., & Ivison, R. J. 2017, *MNRAS*, **470**, 401
- Roueff, E., Felenbok, P., Black, J. H., & Gry, C. 2002, *A&A*, **384**, 629
- Roueff, E., Loison, J. C., & Hickson, K. M. 2015, *A&A*, **576**, A99
- Ruffle, D. P., Hartquist, T. W., Taylor, S. D., & Williams, D. A. 1997, *MNRAS*, **291**, 235
- Sakai, N., Saruwatari, O., Sakai, T., Takano, S., & Yamamoto, S. 2010, *A&A*, **512**, A31
- Schröder, B., & Sebald, P. 2016, *J. Chem. Phys.*, **144**, 044307
- Semenov, D., Hersant, F., Wakelam, V., et al. 2010, *A&A*, **522**, A42
- Sipilä, O., Caselli, P., & Harju, J. 2013, *A&A*, **554**, A92
- Sipilä, O., Caselli, P., & Harju, J. 2015a, *A&A*, **578**, A55
- Sipilä, O., Harju, J., Caselli, P., & Schlemmer, S. 2015b, *A&A*, **581**, A122
- Sipilä, O., Caselli, P., & Harju, J. 2019a, *A&A*, **631**, A63
- Sipilä, O., Caselli, P., Redaelli, E., Juvela, M., & Bizzocchi, L. 2019b, *MNRAS*, **487**, 1269
- Smith, D., & Adams, N. G. 1980, *ApJ*, **242**, 424
- Taniguchi, K., Herbst, E., Ozeki, H., & Saito, M. 2019, *ApJ*, **884**, 167
- van Dishoeck, E. F., & Black, J. H. 1988, *ApJ*, **334**, 771
- Visser, R., van Dishoeck, E. F., & Black, J. H. 2009, *A&A*, **503**, 323
- Wakelam, V., Loison, J. C., Herbst, E., et al. 2009, *A&A*, **495**, 513
- Wakelam, V., Loison, J. C., Herbst, E., et al. 2015, *ApJS*, **217**, 20
- Wampfler, S. F., Jørgensen, J. K., Bizzarro, M., & Bisschop, S. E. 2014, *A&A*, **572**, A24
- Watson, W. D., Anicich, V. G., & Huntress, W. T., J. 1976, *ApJ*, **205**, L165
- Wilson, T. L., & Rood, R. 1994, *ARA&A*, **32**, 191
- Yan, Y. T., Zhang, J. S., Henkel, C., et al. 2019, *ApJ*, **877**, 154
- Zeng, S., Jiménez-Serra, I., Cosentino, G., et al. 2017, *A&A*, **603**, A22
- Zhang, X.-N., Shi, D.-H., Sun, J.-F., & Zhu, Z.-L. 2011, *Chin. Phys. B*, **20**, 043105

Appendix A: Comparison with existing fractionation procedure and chemical models

In this appendix, we compare the results of our chemical model with other results already published in the literature. Firstly, in Appendix A.1, we analyse the fractionation procedures in the implementation of the ^{13}C chemistry and compare with the method used in Roueff et al. (2015). Secondly, in Appendix A.2 we compare our results to the $^{12}\text{C}/^{13}\text{C}$ ratios predicted by Furuya et al. (2011).

A.1. Comparison with Roueff et al. (2015) fractionation procedure

The settling of fractionation reactions involving specific isotopic exchange represents the first important step that has to be completed by the fractionation of the various reactions involving carbon containing molecules, as described in Sect. 2.2. Such a procedure is not unequivocal when several carbon atoms are involved in a chemical reaction. We carefully analysed and compared the present method to the study performed by Roueff et al. (2015) for three different initial conditions in order to test the robustness of our findings. In particular, we used the initial conditions of this work (fiducial model with $n_{\text{H}} = 2 \times 10^4 \text{ cm}^{-3}$ and a temperature of 10 K), and those for model (a) and model (b) described in Table 4 of Roueff et al. (2015) (starless and pre-stellar core conditions, respectively). The results of the comparison are shown in Tables A.1–A.3, for the initial conditions of this work, model (a) and model (b), respectively. The tests are performed on the steady state results of the gas-phase model, as Roueff et al. (2015) did not consider surface reactions. Moreover, they restricted carbon-containing molecules to three carbon atoms, and included up to one ^{13}C in each molecule.

We first ran the chemical network used in Roueff et al. (2015) by suppressing the substituted ^{15}N nitrogen species but keeping the deuterated components. We realised that reactions involving two carbon-containing molecules, which could lead to two other different carbon-containing molecules, could be fractionated differently, according to the chemical mechanism involved. Let us consider the reaction $\text{AC} + \text{BC} \rightarrow \text{A}'\text{C} + \text{B}'\text{C}$. The reaction $\text{A}^{13}\text{C} + \text{BC}$ may then lead to $\text{A}'^{13}\text{C} + \text{B}'\text{C}$ if the reaction proceeds directly, with the same reaction rate coefficient as for the initial reaction. However, if an intermediate complex is occurring, a redistribution of ^{13}C can take place and the reaction may lead to a complete scrambling of the carbon atoms. In this case, an additional channel $\text{A}'\text{C} + \text{B}'^{13}\text{C}$ can be open, and then we assume that each channel occurs with the half value of the rate. The fractionation procedure used in Roueff et al. (2015) did not include this possibility. We thus compare (in Cols. 2 and 3 of the Tables in this section) the role of such scrambling possibilities in

the $^{12}\text{C}/^{13}\text{C}$ ratios of several observed molecules. For example, Table A.1 shows that some ratios are more sensitive than others to this assumption, H_2CO and HNC being particularly sensitive. The introduction of full scrambling leads to a reduction of the $^{12}\text{C}/^{13}\text{C}$ ratio when the ^{13}C isotopologue is found to be diluted in the non-scrambling approach. However, the lower ratios (e.g. for CO , HCO^+) are not affected by this mechanism.

An additional test was performed by using the same chemical network with the additional assumption that the fractionation of ^{13}C acts only on molecules containing a single carbon. The fourth column reports the results from this model, including systematic scrambling as described previously. The fifth column displays the results obtained with the chemical network used in this work, described in Sect. 2.2, assuming, as above, that the fractionation of ^{13}C acts only on molecules containing a single carbon. We see that the results are in a reasonable agreement, with some small differences. These can be attributed to the additional sampling of the reactions made in the present study where charge exchange reactions are quoted specifically. An additional difference between the two treatments concerns the omission of the reactions between two ^{13}C substituted reactants in the test results reported in Col. 5, whereas these reactions are taken into account in the tests reported in Cols. 2–4. All together, we conclude that the main trends of the isotopic ratios are preserved in the different hypotheses made to build the isotopic chemistry, but we indeed acknowledge the unavoidable remaining uncertainties of any systematic procedure.

A.2. Comparison with the previous model of Furuya et al. (2011)

Furuya et al. (2011) studied the behaviour of $^{12}\text{C}/^{13}\text{C}$ for CCH and CCS with a gas-grain chemical model. In particular, their work was based on the study of isotopomer fractionation, that is the abundance ratio between the variants of a given species where the ^{13}C position is allowed to vary. They introduced as isotopic exchange reactions only (1) and (2) of Table 1. Moreover, they did not consider multiple ^{13}C species, contrary to our fractionation procedure, which includes up to three ^{13}C in molecules. Figure A.1 shows the abundances and $^{12}\text{C}/^{13}\text{C}$ ratios predicted by the present model for the same molecules studied by Furuya et al. (2011) in their Fig. 1, for the same physical conditions. We did not include HC_3N since we cut the chemistry to five atom-containing molecules, and the results for this molecule could be biased by this assumption. The general time-dependence of CO , C , C^+ , and HCO^+ is well reproduced in our model. The small differences are likely to be due to the introduction of new possible isotopic exchange reactions in our model that are efficient at low temperatures (like those for CN , C_2 , CS , and C_3).

Table A.1. Comparison between the fractionation procedure used in this work and the one by Roueff et al. (2015): steady state $^{12}\text{C}/^{13}\text{C}$ ratios of different molecular species in a chemical model adopting the initial conditions of the fiducial model of this work.

$^{12}\text{C}/^{13}\text{C}$ ratio	Without scrambling	Full scrambling	1C-molecule	1C-molecule (this work)
$^{12}\text{C}/^{13}\text{C}$	69.0	69.0	69.7	75.8
$^{12}\text{CH}/^{13}\text{CH}$	296.2	277.0	287.0	304.0
$^{12}\text{CO}/^{13}\text{CO}$	68.2	68.2	68.2	68.4
$\text{H}_2^{12}\text{CO}/\text{H}_2^{13}\text{CO}$	304.6	195.6	299.6	307.5
$^{12}\text{CN}/^{13}\text{CN}$	104.3	90.6	204.2	287.4
$\text{H}^{12}\text{CN}/\text{H}^{13}\text{CN}$	271.0	130.6	299.3	283.5
$\text{HN}^{12}\text{C}/\text{HN}^{13}\text{C}$	295.1	128.6	321.6	283.8
$^{12}\text{CS}/^{13}\text{CS}$	85.5	78.1	87.0	244.6
$\text{H}^{12}\text{CO}^+/\text{H}^{13}\text{CO}^+$	28.3	28.3	28.3	26.0

Notes. Column 2 represents the results obtained with the same chemical network of Roueff et al. (2015) by suppressing the substituted ^{15}N -nitrogen species but keeping the deuterated components, and without considering a full scrambling of carbon atom in molecules, as described in Appendix A.1. Column 3 is the same as Col. 2, but considers full scrambling. Column 4 represents the results obtained with the same network as Col. 3, but considers inclusion of ^{13}C only in molecules containing one carbon atom. Column 5 shows the corresponding results obtained with the chemical network developed for this work (Sect. 2.2), reduced with the same assumption made for Col. 4.

Table A.2. Same as Table A.1, but adopting the initial conditions of model (a) in Roueff et al. (2015), corresponding to a starless core.

$^{12}\text{C}/^{13}\text{C}$ ratio	Without scrambling	Full scrambling	1C-molecule	1C-molecule (this work)
$^{12}\text{C}/^{13}\text{C}$	102.1	101.7	115.7	193.5
$^{12}\text{CH}/^{13}\text{CH}$	487.2	465.3	412.1	416.9
$^{12}\text{CO}/^{13}\text{CO}$	68.0	68.0	67.8	68.0
$\text{H}_2^{12}\text{CO}/\text{H}_2^{13}\text{CO}$	490.5	382.9	422.6	418.1
$^{12}\text{CN}/^{13}\text{CN}$	216.9	191.5	291.8	402.4
$\text{H}^{12}\text{CN}/\text{H}^{13}\text{CN}$	266.7	198.4	284.0	276.5
$\text{HN}^{12}\text{C}/\text{HN}^{13}\text{C}$	345.6	212.8	321.3	273.8
$^{12}\text{CS}/^{13}\text{CS}$	144.0	135.3	159.1	364.2
$\text{H}^{12}\text{CO}^+/\text{H}^{13}\text{CO}^+$	45.5	45.6	47.1	40.6

Table A.3. Same as Table A.1, but adopting the initial conditions of model (b) in Roueff et al. (2015), corresponding to a pre-stellar core.

$^{12}\text{C}/^{13}\text{C}$ ratio	Without scrambling	Full scrambling	1C-molecule	1C-molecule (this work)
$^{12}\text{C}/^{13}\text{C}$	136.7	135.4	171.1	263.7
$^{12}\text{CH}/^{13}\text{CH}$	445.9	432.3	380.2	343.6
$^{12}\text{CO}/^{13}\text{CO}$	67.8	67.8	67.4	68.0
$\text{H}_2^{12}\text{CO}/\text{H}_2^{13}\text{CO}$	443.3	334.0	382.4	342.5
$^{12}\text{CN}/^{13}\text{CN}$	329.3	204.4	332.4	337.1
$\text{H}^{12}\text{CN}/\text{H}^{13}\text{CN}$	292.5	162.2	290.6	251.8
$\text{HN}^{12}\text{C}/\text{HN}^{13}\text{C}$	304.4	147.2	285.2	247.2
$^{12}\text{CS}/^{13}\text{CS}$	230.0	171.8	257.1	327.1
$\text{H}^{12}\text{CO}^+/\text{H}^{13}\text{CO}^+$	44.5	44.5	43.7	39.4

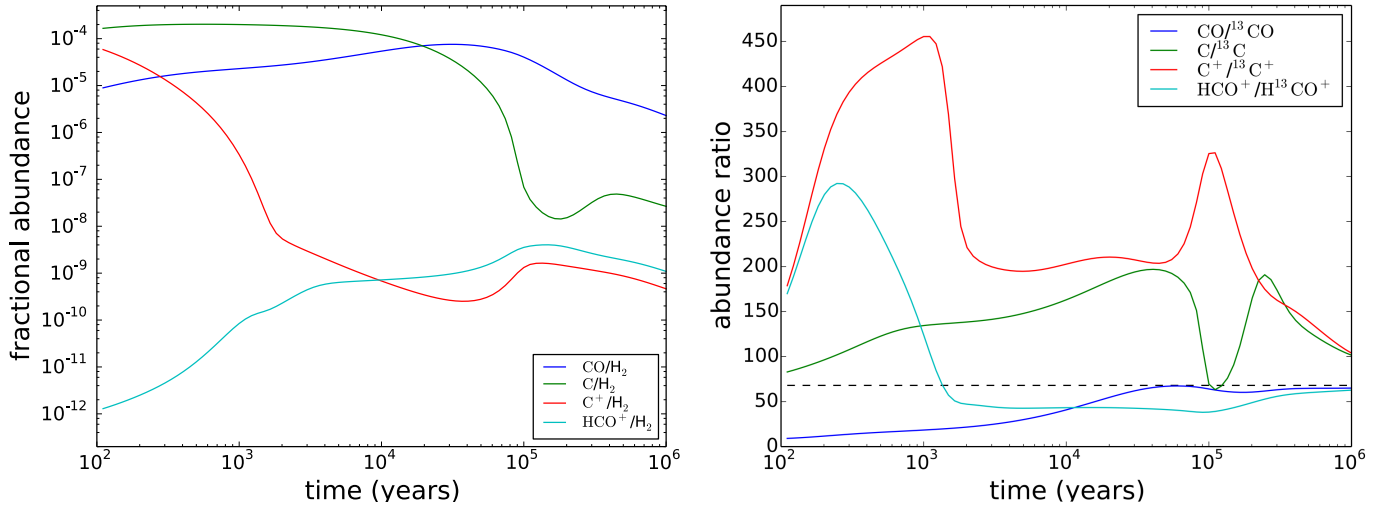


Fig. A.1. Abundances (*left panel*) and $^{12}\text{C}/^{13}\text{C}$ ratios (*right panel*) from our chemical model using a density of 10^5 cm^{-3} and temperature of 10 K (same as [Furuya et al. 2011](#)). In the *right panel*, the black horizontal dashed line represents the initial $^{12}\text{C}/^{13}\text{C}$ ratio of 68.

Appendix B: Parameter-space exploration of CO, HCO^+ , H_2CO

In this appendix, we show the $^{12}\text{C}/^{13}\text{C}$ ratio of CO, HCO^+ , and H_2CO as a function of n_{H} and for different temperatures

(Figs. B.1–B.3, respectively). In particular, we perform the same parameter-space exploration as that done for CN, HCN, and HNC in Sect. 3.2.

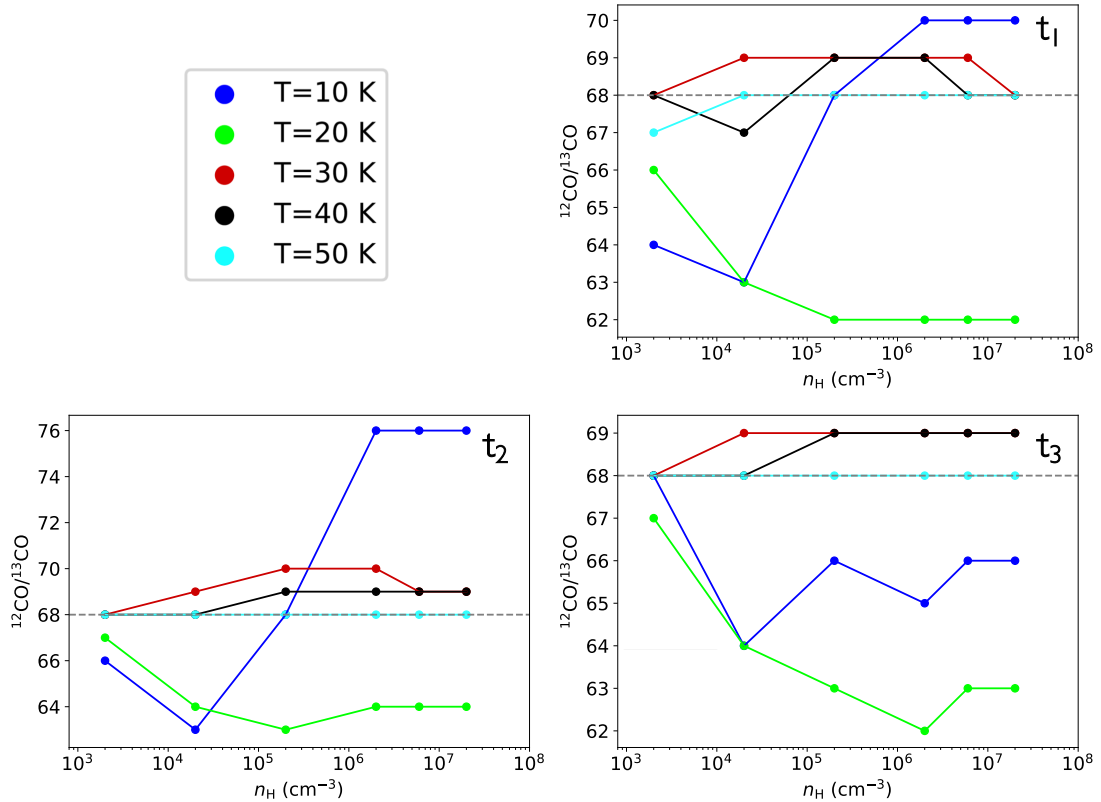


Fig. B.1. $^{12}\text{CO}/^{13}\text{CO}$ ratio as a function of n_{H} , for different temperatures, at t_1 (*top-right panel*), t_2 (*bottom-left panel*), and t_3 (*bottom-right panel*). The black horizontal dashed line represents the initial $^{12}\text{C}/^{13}\text{C}$ ratio of 68.

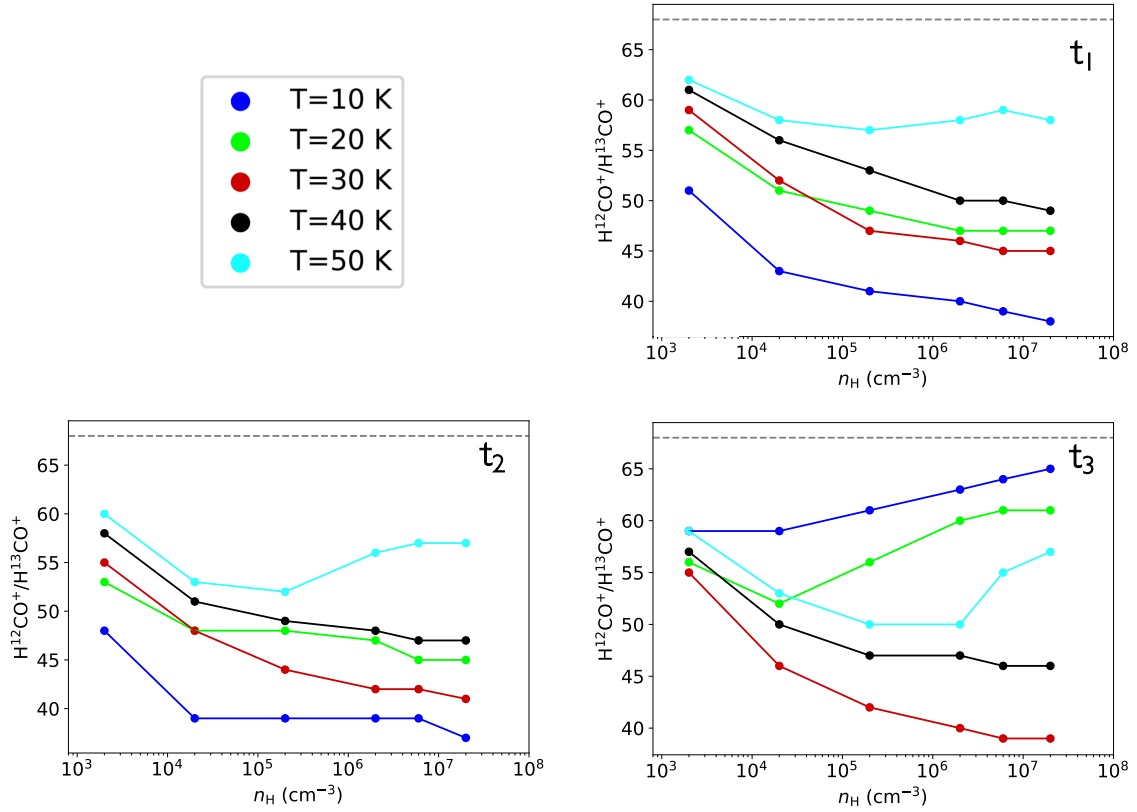


Fig. B.2. As Fig. B.1, but for $\text{H}^{12}\text{CO}^+/\text{H}^{13}\text{CO}^+$.

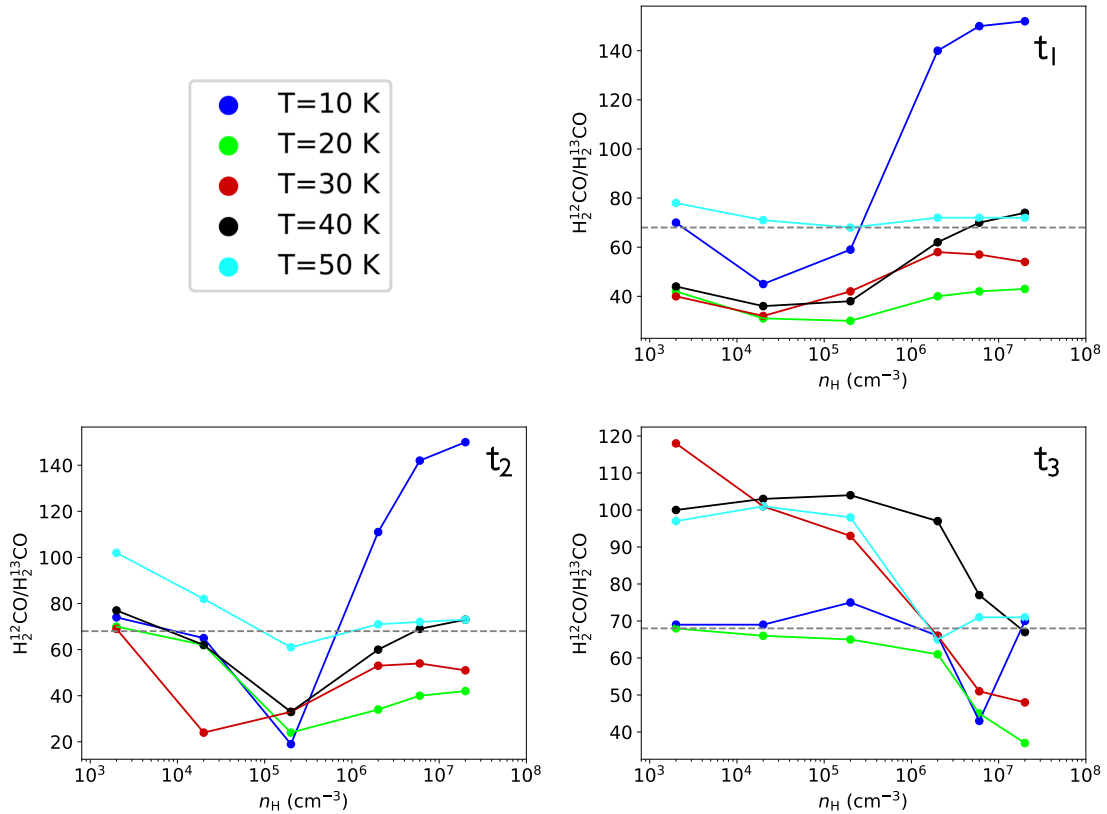


Fig. B.3. As Fig. B.1, but for $\text{H}_2^{12}\text{CO}/\text{H}_2^{13}\text{CO}$.

Appendix C: Main formation and destruction pathways for different values of ζ

In this appendix, the main destruction and formation pathways of various species for ζ_{low} and ζ_{high} are shown (Figs. C.1 and C.2,

respectively). The main discussion about the different results obtained assuming a different ζ is given in Sect. 3.2.3.

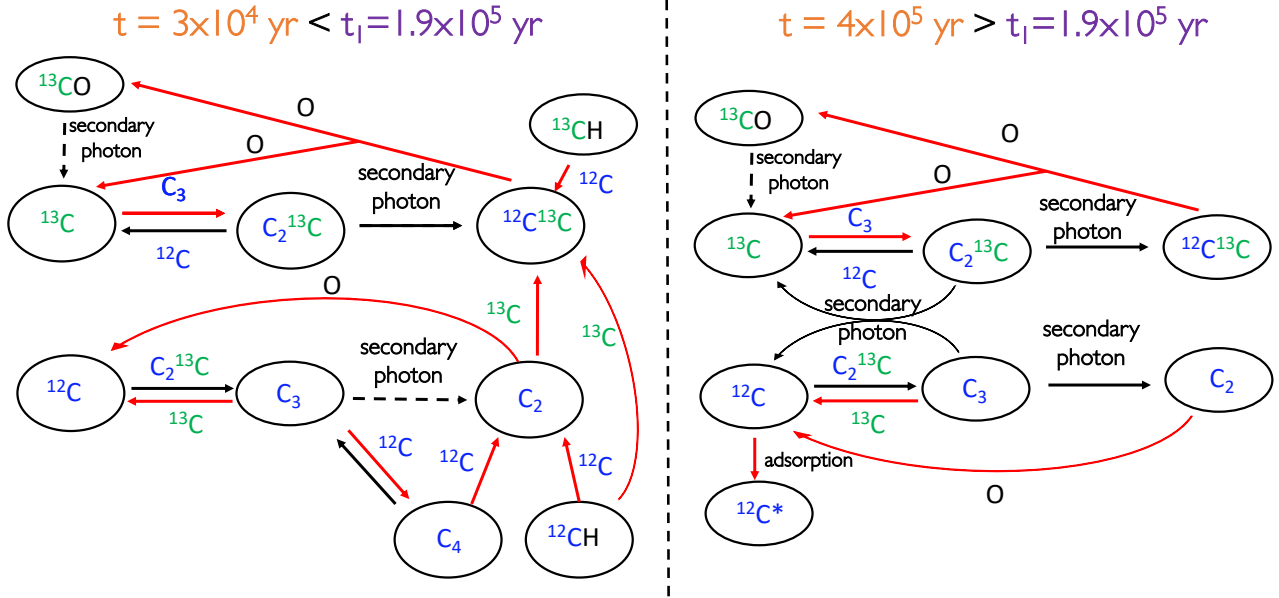


Fig. C.1. Chemical pathways that distribute the two carbon isotopes in atomic carbon, C_2 and C_3 at 3×10^4 yr (left panel) and 4×10^5 yr (right panel), for the fiducial model with a cosmic-ray ionisation rate of $1.3 \times 10^{-18} \text{ s}^{-1}$. Main creation and destruction reactions are highlighted in red, ^{12}C is represented in blue, and ^{13}C is represented in green. In this plot, the dashed black reactions are the less important ones.

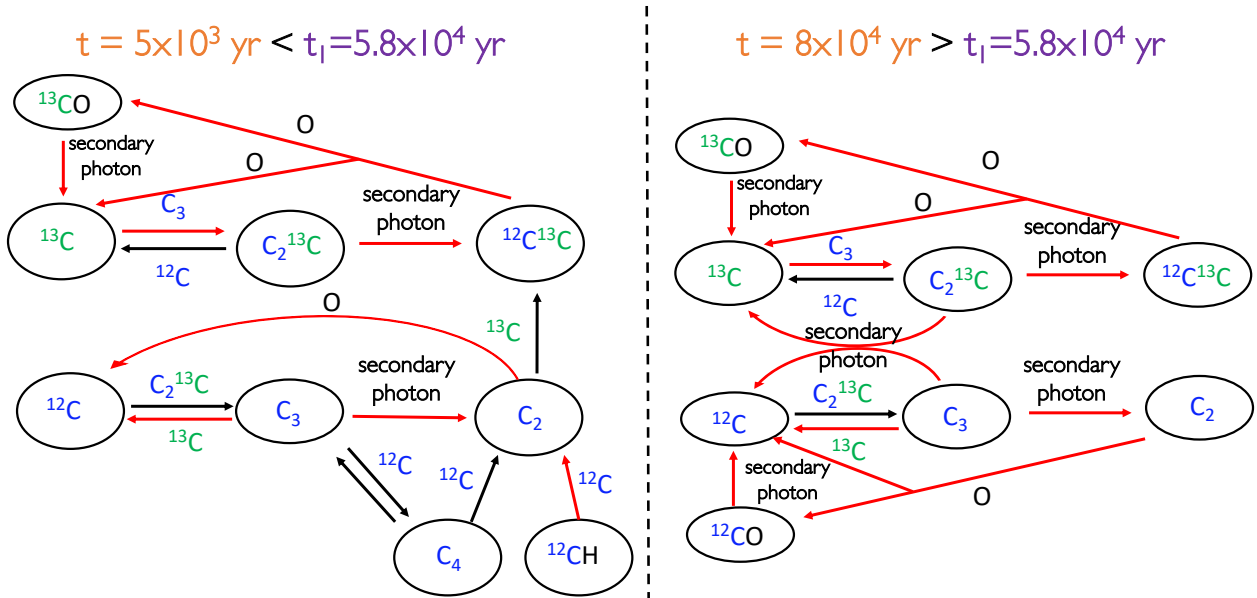


Fig. C.2. Chemical pathways that distribute the two carbon isotopes in atomic carbon, C_2 and C_3 at 5×10^3 yr (left panel) and 8×10^4 yr (right panel), for the fiducial model with a cosmic-ray ionisation rate of $1.3 \times 10^{-16} \text{ s}^{-1}$. Main creation and destruction reactions are highlighted in red, ^{12}C is represented in blue and ^{13}C is represented in green.